

POLITECNICO DI TORINO

Corso di Laurea Magistrale in Ingegneria Aerospaziale



**Politecnico  
di Torino**



**MAX-PLANCK-INSTITUT  
FÜR PLASMAPHYSIK**

Tesi di Laurea Magistrale

**Multi-physics lumped modeling for  
a MW-class heat flux component  
equipped with micro-channels**

**Supervisor**

Prof. Laura SAVOLDI

Ms. Rosa DIFONZO

Dr. Joris FELLINGER

**Candidato**

Francesco CARRONE

Anno Accademico 2022/2023

# Abstract

Nuclear fusion reactors, such as the experimental stellarator Wendelstein 7-X at the Max Planck Institute for Plasma Physics (IPP) – Greifswald represent a promising solution for decarbonizing the power sector in the second half of the century. In pursuit of this objective, the cooling system of the W7-X divertor, specifically developed to handle high heat fluxes, is presently undergoing design improvements.

A new concept has been proposed for this cooling system, which involves a network of parallel arrays of sub-millimeter rectangular micro-channels (MCs) on each 0.1m X 0.1m tile covering the divertor surface. The micro-channels are obtained using Additive Manufacturing techniques in a galvanized copper heat sink substrate, with tungsten as the plasma-facing material and water used for cooling.

To reduce the high computational cost of thermal-hydraulic simulations for the such cooling system, a lumped modeling approach has been built in previous studies. This involves replacing a group of hydraulic parallel micro-channels (MCs) with a properly calibrated thermal-hydraulic porous strip (PS) through the application of a 5 MW/m<sup>2</sup> heat flux and inlet mass flow rate of 50 l/min for the entire tile. This study was performed in accordance with the constraints of the GLADIS facility at IPP. The aim of this thesis is to verify the PS-model is also suitable for the thermo-mechanical stress evaluation; to do that, results obtained with arrays equipped with MCs and PS are compared in different conditions. Since the heat sink substrate and the plasma-facing tile are bonded, the thermo-mechanical problem in bonded structures is investigated under the free surface edge boundary condition, which is the most critical for structural integrity. In this scenario, the interfacial delamination and shear stresses are analyzed in the elastic regime. First, a simple case with the same layer structure of the tile is modeled, and the results are compared to the literature; then the results are compared to those obtained from arrays with MCs and PS with similar geometry. The evaluation is conducted first by applying a uniform temperature load, and then by using temperature maps extracted from the thermal-hydraulic simulations. The computational fluid dynamics and finite element analyses are performed using the STAR-CCM+ software by Siemens.

The PS-model, which estimates higher temperatures, overestimates the delamination and shear stresses at the free edge, highlighting its conservative nature compared to the MCs-model. Moreover, the findings of this study indicate that micro-channels (MCs) and porous blocks, located near the bond interface, contribute to high-stress fluctuations that could lead to the interface debonding, suggesting that thickness needs to be increased. Results from both models reveal nearly identical interfacial stress predictions at the free surface edge.

As a final contribution to the project, the feasibility of hydraulically connecting the tiles in a divertor unit target module, while taking operational constraints into consideration, is also evaluated.



# List of Contents

|         |   |    |
|---------|---|----|
| 1       | Introduction.....   | 1  |
| 1.1     | W7-X and its divertor description                                     | 2  |
| 1.2     | The micro-channel cooling configuration for the single tile           | 4  |
| 1.3     | Lumped tile modeling with equivalent porous strips                    | 5  |
| 1.4     | Aims of the study   | 7  |
| 2       | The thermo-mechanical issue in Plasma Facing Components.....          | 8  |
| 2.1     | Physics of the problem  | 8  |
| 2.2     | Review of analytical models of bi-material joint structures           | 9  |
| 2.2.1   | Interfacial stresses analytic prediction                              | 9  |
| 2.2.2   | The singularity at the free surface edge                              | 12 |
| 2.3     | Numerical Models Review   | 14 |
| 2.4     | A relevant case study: thermo-mechanical simulation of a simple array | 16 |
| 2.4.1   | Geometry and Material properties                                      | 16 |
| 2.4.2   | Constraints and Temperature Load                                      | 18 |
| 2.4.3   | Mesh  | 19 |
| 2.4.4   | Simulation Results and Discussion                                     | 19 |
| 3       | The thermo-mechanical modeling of a tile array .....                  | 23 |
| 3.1     | From the tile to the single array                                     | 23 |
| 3.2     | Tile array equipped with MCs  | 23 |
| 3.2.1   | Geometry and material properties                                      | 23 |
| 3.2.2   | Constraints and Temperature Load                                      | 24 |
| 3.2.3   | Mesh  | 25 |
| 3.2.4   | Simulation Results and Discussion                                     | 25 |
| 3.2.4.1 | Thickness mesh refinement   | 25 |

|         |  |    |
|---------|--|----|
| 3.2.4.2 | Free edge mesh refinement                                      | 28 |
| 3.3     | Tile array equipped with PS                                    | 29 |
| 3.3.1   | Geometry and material properties                               | 29 |
| 3.3.2   | Constraints and Temperature Load                               | 30 |
| 3.3.3   | Mesh   | 30 |
| 3.3.4   | Simulation Results and Discussion                              | 30 |
| 3.4     | Discussion on Models comparison                                | 32 |
| 3.4.1   | Uniform specified temperature                                  | 32 |
| 3.4.2   | Temperature maps   | 32 |
| 3.5     | Application of the lumped model                                | 34 |
| 4       | MCs tiles connection in an entire divertor target module ..... | 36 |
| 4.1     | Tile design improvement  | 36 |
| 4.2     | Operational constraints  | 38 |
| 4.3     | Hydraulic simulation – PS half tile                            | 38 |
| 4.4     | Tiles connection proposals                                     | 40 |
| 4.5     | Boiling check  | 43 |
| 4.5.1   | Conjugate heat transfer analyses                               | 45 |
| 4.6     | Final configuration  | 48 |
| 5       | Conclusions.....   | 49 |
| 5.1     | Future perspectives  | 50 |
|         | Bibliography .....   | 51 |
|         | APPENDIX A: Lumped model accuracy                              | 56 |

# List of Figures

- Figure 1** Schematic diagram of the W7-X with the 50 non-planar (red) and 20 planar (orange) superconducting coils, taken from [5]. 2
- Figure 2** W7-X five-fold modules with its 10 divertor units, 5 upper and 5 lower. The divertor targets intersecting the magnetic islands are shown, taken from [11]. 3
- Figure 3** Main target areas of one divertor unit, showing the vertical and horizontal TMs which define the main pumping gap<sup>(1)</sup>, taken from [8]. 3
- Figure 4** Schematic view of the MCs cooling structure of half water-cooled divertor tile, taken from [13]. 5
- Figure 5** Subdomain of 6 MCs (a) and the equivalent PS block (b), with their cooling paths, respectively (c,d), taken from [13]. 6
- Figure 6** Schematic 2D view of a duplex bond joint structure of a PFC. 8
- Figure 7** Stress analysis model, where  $\tau(x)$  are the interfacial shear stresses,  $p(x)$  are the interfacial peeling stresses along the x-direction,  $T_x$  is the longitudinal shear force;  $M_{1,2}(x)$  are the bending moments. 10
- Figure 8** Peeling stresses (MPa) obtained for a Silicon/Aluminium system, taken from [31]. 11
- Figure 9** Shearing stresses (MPa) obtained for a Silicon/Aluminum system, taken from [31]. 12
- Figure 10** General configuration of a duplex bond joint of a PFC at the free edge. 13
- Figure 11** Interfacial normal stresses near the free surface edge obtained analytically for different material combinations, taken from [22]. 14
- Figure 12** Comparison of interfacial normal stresses predicted by an analytical method with those by FEM, taken from [36]. 15
- Figure 13** Comparison of interfacial shear stresses predicted by an analytical method with those by FEM, taken from [36]. 16
- Figure 14** Schematic 3D view of the simple array. 17

- Figure 15** Constraints applied to the simple array; all the other surfaces or nodes are free of any constraints. 18
- Figure 16** Tetrahedral mesh generated on the simple array with a mesh refinement zoom applied on the free surface edge of the bond interface. 19
- Figure 17** Simple array with a zoom on the bond interface; peeling stresses are extracted along the line closer to the constrained edge while shear stresses are extracted along the central line. 20
- Figure 19** Delamination or peeling stresses along a line on the bond interface (simple array); a focus on the delamination peak increasing with the mesh base size decreasing is reported. 21
- Figure 20** Shear stresses along a line on the bond interface (simple array); a focus on the zero-boundary condition and the shear stress peak increasing with the mesh base size decreasing is reported. 22
- Figure 21** Schematic 3D view of MCs-array (outlet manifold view). 24
- Figure 22** Schematic 3D view of MCs-array (inlet manifold view) with a zoom on the MCs structure. 24
- Figure 23** Mesh refinement applied on the thickness between the bond interface and the MCs. 25
- Figure 24** Thickness mesh refinement (MCs-array), delamination stresses comparison: median (on the left) and delamination peak (on the right). 26
- Figure 25** Thickness mesh refinement (MCs-array), shear stresses comparison: median (on the left) and zero-shear stress value (on the right). 26
- Figure 26** Delamination or peeling stresses along a line on the bond interface (MCs-array); thickness mesh refinement applied only. 27
- Figure 27** Shear stresses along a line on the bond interface (MCs-array); thickness mesh refinement applied only. 28
- Figure 28** MCs-array, delamination or peeling (on the left) and shear (on the right) stress: zoom on the free surface edge region highlighting the mesh refinement effect. 29
- Figure 29** Schematic 3D view PS-array (outlet manifold view). 29
- Figure 30** Schematic 3D view PS-array (inlet manifold view) with a zoom on the PS blocks structure. 30

- Figure 31** Delamination or peeling stresses along a line on the bond interface (PS-array). 31
- Figure 32** Shear stresses along a line on the bond interface (PS-array). 31
- Figure 33** Delamination or peeling (on the left) and shear (on the right) stress: zoom on the free surface edge region comparing the simple, MCs and PS arrays with a uniform temperature load applied. 32
- Figure 34** Temperature maps applied on the MCs-array (top figure) and on the PS-array (bottom figure) as thermal load. 33
- Figure 35** Delamination or peeling (on the left) and shear (on the right) stress: zoom on the free surface edge region comparing the MCs and PS arrays with a temperature map applied. 34
- Figure 36** Delamination or peeling stresses along a line on the bond interface (PS-array), with two thickness increases between the PS blocks and the bond interface. 35
- Figure 37** Shear stresses along a line on the bond interface (PS-array), with two thickness increases between the PS blocks and the bond interface. 35
- Figure 38** Last tile array, with the manifold inlet and outlet cut; a zoom of the new HSS thickness is reported, in respect of the distance from the outlet section. 37
- Figure 39** Tile array with a zoom on the new thickness between MCs and bond interface. 37
- Figure 40** Half-tile (only fluid) equipped with PS blocks. 39
- Figure 41** Hydraulic characteristics computing the pressure drop for different inlet mass flow rate values on a half-tile equipped with PS blocks. 40
- Figure 42** Proposal 1: 6 parallel paths connecting 4 tiles in series (3 poloidally and 1 toroidally); each tile is represented by a blue block, while each parallel path is by a red arrow. 42
- Figure 43** Proposal 2: 4 parallel paths connecting 6 tiles in series (4 poloidally and 2 toroidally); each tile is represented by a blue block, while each parallel path is by a red arrow. 42
- Figure 44** Proposal 3: 8 parallel paths connecting 3 tiles in series poloidally; each tile is represented by a blue block, while each parallel path is by a red arrow. 43

- Figure 45** Proposal 4: 4 parallel paths connecting 6 tiles in series poloidally; each tile is represented by a blue block, while each parallel path is by a red arrow. 43
- Figure 46** Water repartitioning, among the manifold, in a half PS tile with an inlet mass flow rate of 595 g/s. 44
- Figure 47** Last tile array with symmetry plane boundary condition imposed only on the inlet manifold surface. 46
- Figure 48** Central tile array with symmetry plane boundary condition imposed on the inlet manifold and outlet manifold surfaces. 46
- Figure 49**  $\Delta T_{\text{boiling}} = T_{\text{wall}} - T_{\text{sat}}$  computed on the least uncooled central array with a  $m_{\text{frinlet}}$  of 27.7 g/s and an imposed heat flux of 14 MW/m<sup>2</sup> on the heated surface. 47
- Figure 50** Hydraulic scheme of Proposal 3 for the TM, composed of 8 parallel paths connecting 3 tiles in series poloidally, requiring two pumps of 5 kg/s each; the scheme is represented considering the configuration symmetry. 48
- Figure 51** Mass flow repartition in the different PS and MC (grouped by 6) on a single array with an applied heat load of 5, 10, 15 MW/m<sup>2</sup>. 57
- Figure 52** Average temperature increase (with respect of the inlet water temperature) on the heated surface along a single equipped with MCs and PS, subjected to a heat load of 5, 10, 15 MW/m<sup>2</sup>. 57

# List of Tables

|   |    |
|---|----|
| <b>Table 1</b> Thermo-mechanical properties of tungsten and galvanized copper. .  | 17 |
| <b>Table 2</b> Porous coefficients coming out from the PS calibration, taken from Ref. [13].  | 40 |
| <b>Table 3</b> Inlet mass flow rates computed for the last tile array and central tile array.   | 44 |
| <b>Table 4</b> Summary of the different tiles connection proposals in a target module; the limits of the infrastructure not respected are highlighted in red. | 48 |

# List of Abbreviations

## Acronyms

|     |                              |
|-----|------------------------------|
| AM  | Additive manufacturing       |
| BC  | Boundary conditions          |
| CHF | Critical heat flux           |
| CFD | Computational fluid dynamics |
| FEM | Finite element modeling      |
| HHF | High heat flux               |
| HSS | Heat sink substrate          |
| MC  | Micro-channel                |
| PFM | Plasma-facing material       |
| PFC | Plasma-facing component      |
| PS  | Porous strip                 |
| TE  | Target element               |
| TM  | Target module                |

| <b>Symbols</b> | <b>Description</b>            | <b>Units</b>   |
|----------------|-------------------------------|----------------|
| $\alpha$       | Thermal expansion coefficient | 1/K            |
| A              | Area                          | m <sup>2</sup> |
| $c_p$          | Specific heat                 | J/kg/K         |
| E              | Young's modulus               | GPa            |
| H              | Enthalpy                      | W/s            |
| k              | Thermal conductivity          | W/m/K          |
| $\dot{m}$      | Mass flow rate                | g/s            |

|                           |                              |                   |
|---------------------------|------------------------------|-------------------|
| $m\dot{r}_{\text{inlet}}$ | Inlet mass flow rate         | g/s               |
| $\nu$                     | Poisson coefficient          | -                 |
| $p$                       | Interfacial peeling stresses | MPa               |
| $Q$                       | Heat flux                    | W/m <sup>2</sup>  |
| $\rho$                    | Density                      | kg/m <sup>3</sup> |
| $\bar{\sigma}$            | Stress tensor                | MPa               |
| $\tau$                    | Interfacial shear stresses   | MPa               |
| $T$                       | Temperature                  | K                 |



# Chapter 1

## Introduction

Fusion energy could in principle in the long run play a role in decarbonizing our economies, as it can potentially provide a nearly limitless source of clean and sustainable energy [1].

Fusion reaction [2] is possible through the fusion between two hydrogen isotopes, deuterium, and tritium. To make the reaction self-sustained, high-temperature and high-density energy confinement are required. The confinement of the plasma is one of the principal technological issues of fusion and the main strategies are inertial confinement and magnetic confinement. Considering the second one, the two configurations are tokamak and stellarator.

The stellarators [3] are characterized by coils surrounding the plasma that generate rotational transform without requiring plasma currents; for this reason, these devices are inherently stationary.

The world's largest stellarator built is the Wendelstein 7-X (W7-X) at the Max Planck Institute for Plasma Physics (IPP) in Greifswald, Germany. Its aim is to demonstrate the suitability of reaching plasma equilibrium and confinement of a quality comparable with that of a tokamak of the same size, with the benefit of avoiding a large current flowing in a tokamak plasma [4]. The magnetic field which confines the plasma is produced by a complex system of coils.

## 1.1 W7-X and its divertor description

The W7-X [5] is characterized by 50 non-planar coils and 20 planar coils connected in series via superconducting bus bars; all coils are bolted to a massive central support ring and fixed by support elements that could be mostly welded, partially bolted, or sliding locally. A schematic view of the W7-X magnetic system is reported in **Figure 1**.

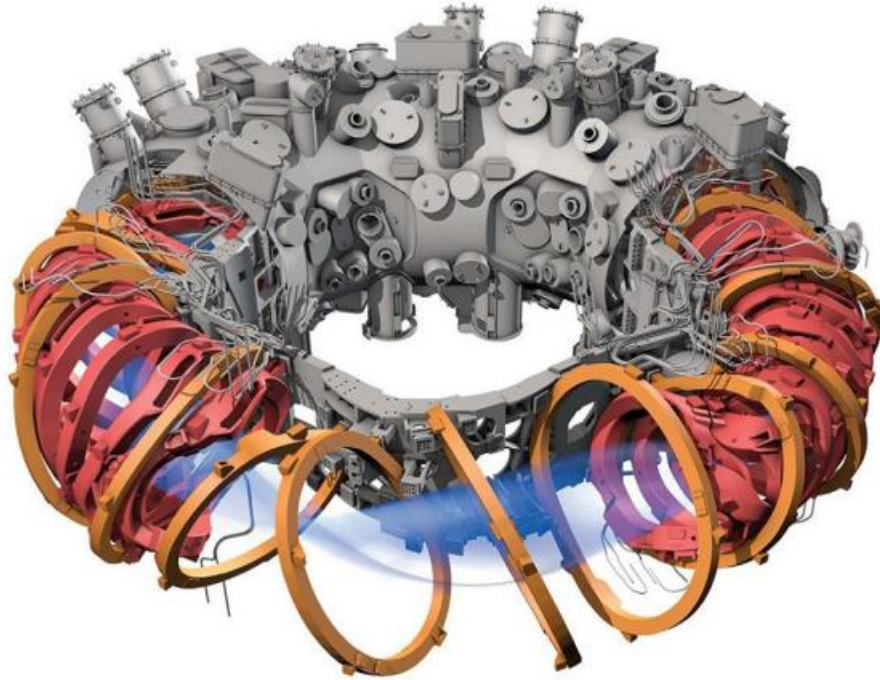


**Figure 1** Schematic diagram of the W7-X with the 50 non-planar (red) and 20 planar (orange) superconducting coils, taken from [5].

In addition to the superconducting magnet system, W7-X is equipped with a high-power heating system and actively water-cooled plasma-facing components (PFCs) including a divertor, which aims to handle the power and particle flux, and to limit the impurity fraction to tolerable levels [6]. The W7-X divertor [7] consists of 10 similar discrete divertor units and is composed of target modules<sup>1</sup>, baffle modules,<sup>2</sup> and the closure of the divertor chamber in the poloidal and toroidal directions. The configuration of the divertor units is visible in **Figure 2**.

---

<sup>1</sup> The areas where the energy is dissipated.

<sup>2</sup> The areas which help to concentrate the neutral flux particles in pumping gap.

The target modules (TMs) [8] are positioned in vertical and horizontal areas, as shown in **Figure 3**, defining the pumping gap; the total surface area of the TMs is  $25.6 \text{ m}^2$ . Each TM is composed of target elements (TEs) of the same length placed onto a support frame and fed with water from manifolds [9]. A target element is made of a CuCrZr copper alloy heat sink armored with carbon fibre reinforced carbon CFC NB31 tiles [10]; it is designed to remove a stationary heat flux, on its main area, of  $10 \text{ MW/m}^2$  for up to 30 minutes, with peaks of maximum  $20 \text{ MW/m}^2$  for up to 10 seconds [9].

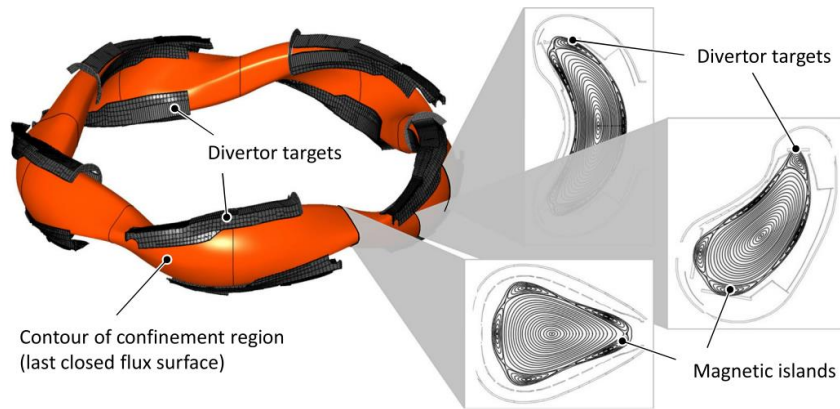


**Figure 2** W7-X five-fold modules with its 10 divertor units, 5 upper and 5 lower. The divertor targets intersecting the magnetic islands are shown, taken from [11].

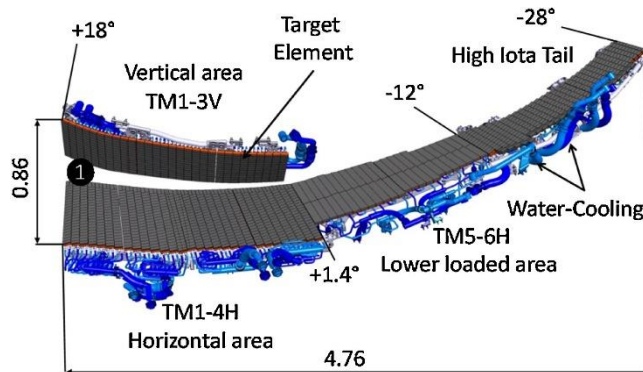


**Figure 3** Main target areas of one divertor unit, showing the vertical and horizontal TMs which define the main pumping gap<sup>(1)</sup>, taken from [8].

## 1.2 The micro-channel cooling configuration for the single tile

The W7-X water-cooled divertor, like other W7-X PFCs, is under refurbishment [12]. In particular, the exploration of alternative and novel cooling solutions is of high interest. The proposal [13] taken into consideration in this work is a network of parallel arrays of micro-channels<sup>3</sup> (MCs); the arrays are connected by Z-manifolds<sup>4</sup>, typically [14] used to connect cooling channels of PFCs. The MCs structure is obtained using Additive Manufacturing (AM) techniques.

The use of MCs has been tested in different applications, such as in microelectronic devices [15] where thermal issues are preponderant. In fusion energy, a similar configuration has been recently proposed for the China Fusion Engineering Test Reactor (CFETR) divertor obtaining good hydrothermal performance [16].

The MCs are beneficial especially for providing a high surface-to-volume ratio [17] but, at the same time, particular attention must be addressed regarding the flow boiling. Indeed, the thermal and hydraulic instabilities caused by the boiling are well known [18], and they can modify the hydrodynamics inside the channels, creating mechanical vibrations which can cause premature critical heat flux (CHF) and finally lead the device damage [19].

The flat tile design (100 mm X 100 mm), which corresponds to a TE, consists of a copper heat sink substrate (HSS) and a tungsten layer that uniformly withstands the heat load. The tungsten thickness is 2 mm. A schematic configuration is reported in **Figure 4**.

The optimal behavior of copper as heat sink material makes it the first choice for water-cooled components in fusion reactors. Recent test campaigns have shown that copper obtained through the electrodeposition technique (galvanized copper) permits to obtain a complex geometry shape (with small cooling channels) and to have good mechanical properties at the same time, due to the high purity and very small grain size [20]. So, in comparison with pure annealed copper, galvanized copper is characterized by larger fatigue life while no

---

<sup>3</sup> Micro-channels are sub-millimeter rectangular channels.

<sup>4</sup> Manifold type characterized by inlet and outlet on the opposite sides, where the fluid flows in the same direction.

difference has been found in terms of thermal properties. In the current study, galvanized copper properties are utilized.

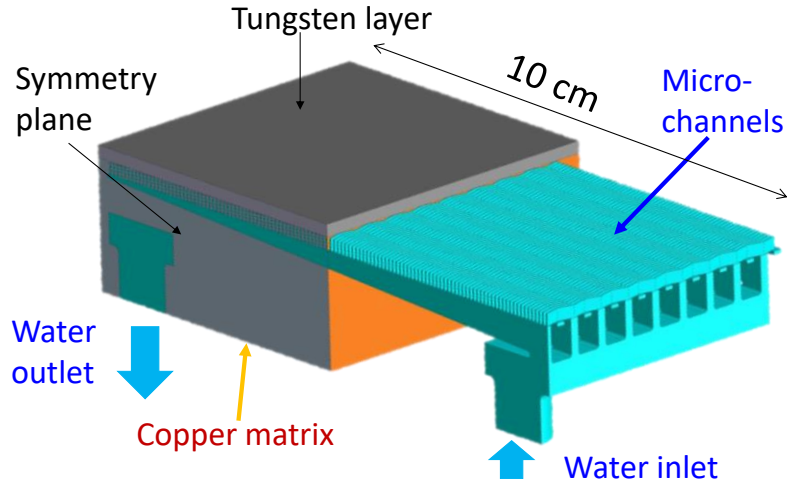


**Figure 4** Schematic view of the MCs cooling structure of half water-cooled divertor tile, taken from [13].

### 1.3 Lumped tile modeling with equivalent porous strips

To analyze the proposed design, Computational Fluid Dynamics (CFD) and Finite Element Modeling (FEM) analyses are required. For components such as the mockup considered in the current study, the conjugate heat transfer problem resolution requires a very intensive numerical effort because of the large computational grid implemented on the high number of MCs inserted in the structure.

To reduce the computational cost, a lumped modeling approach has been adopted. It generally prescribes the development of surrogate models that “lump” the thermal-hydraulic behavior of the original components. In this paragraph, the methodology implemented, and results obtained are shortly reported, but more details can be found in [13].

In this case, the lumped model has been developed by the substitution of a subdomain of 6 MCs connected in parallel, original components, with an equivalent porous strip (PS), surrogate model, as depicted in **Figure 5**. The equivalent PS thermo-hydraulic properties have been calibrated fitting the hydraulic and thermal characteristics of 6 MCs, performing CFD simulations on the introduced subdomains, to reduce the computational cost. Specifically, the

MCs hydraulic characteristics have been fit by the Darcy-Forchheimer formulation computing the viscous and inertial coefficients, while the MCs thermal characteristics have been fit by the thermal power equations computing the anisotropic thermal conductivity coefficients.

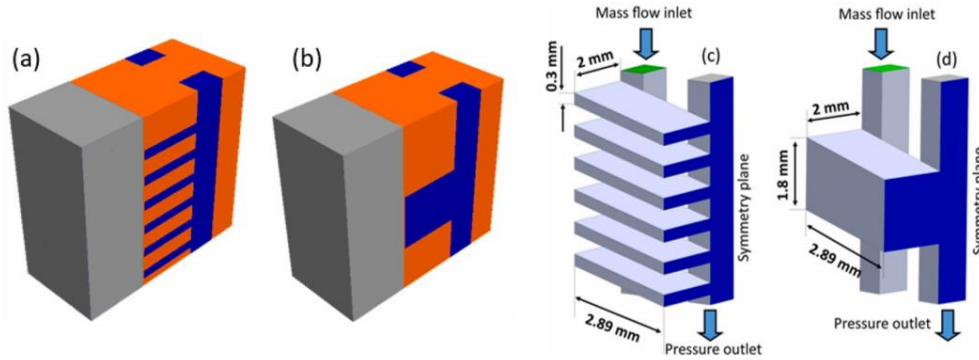


**Figure 5** Subdomain of 6 MCs (a) and the equivalent PS block (b), with their cooling paths, respectively (c,d), taken from [13].

The sub-domain substitution has been also extended to the array scale; in particular, an MCs-array is composed of 120 MCs while a PS-array of 20 PS blocks. The results showed acceptable levels of hydraulic (9%) and thermal (11%) accuracy, comparing the two arrays.

Since the proposed design mockup aims to be tested in the GLADIS facility at IPP, which provides an intense ion beams flux and 50 l/min of subcooled water at 0.75 bar and 27 °C [21], the described calibration has been conducted in accordance with those boundary conditions (BCs), and imposing uniform heat flux of 5 MW/m<sup>2</sup>.

Note that the calibration in [13] was just for methodological purposes, and higher heat fluxes than 5 MW/m<sup>2</sup> could be necessary to apply the model to propose a new divertor configuration; more details are highlighted in APPENDIX A.

## 1.4 Aims of the study

The current study has two principal aims:

1. Verify the PS-model is also suitable for the stress evaluation in comparison with the MCs-array;
2. Evaluate the feasibility of the tiles' hydraulic connection in one target module respecting the operational constraints.

The first aim is addressed through a thermo-mechanical study of the PFCs performing FEM analyses of a relevant case study, with a similar geometry of the MCs and PS arrays. First, the models under consideration are compared by subjecting them to a uniform temperature load. Then, the temperature maps obtained using the boundary conditions used for the PS-array thermo-hydraulic validation (as described in section 1.3) are used to compare the models further.

The second aim allows the critical evaluation of different configurations connecting hydraulically the tiles in series or in parallel. In particular, it's required the flow must stay in a single phase, avoiding boiling; furthermore, the operation constraints prescribe, for the target module, a maximum pressure drop of 15 bar, an inlet mass flow rate of 5 kg/s, provided by a single pump, and a maximum heat load of 15 MW/m<sup>2</sup> in the toroidal direction.

## Chapter 2

# The thermo-mechanical issue in Plasma Facing Components

### 2.1 Physics of the problem

The plasma-facing components (PFCs) of fusion reactors are typically characterized by duplex joint structures, consisting of plasma-facing armour tiles bonded to a metallic heat sink substrate, equipped with channels for heat removal [22]. A schematic 2D view is reported in **Figure 6**.

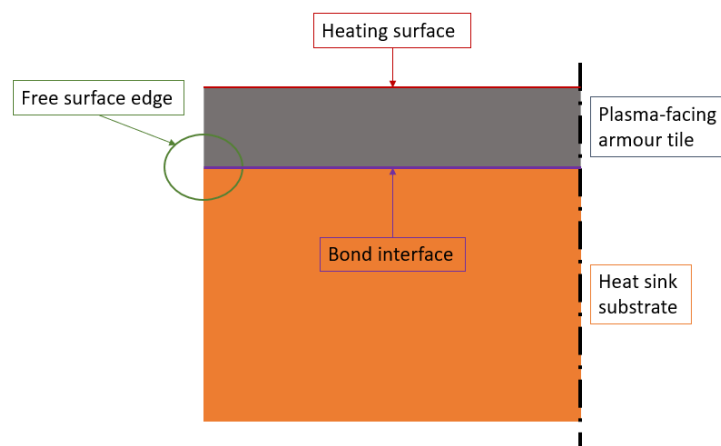


**Figure 6** Schematic 2D view of a duplex bond joint structure of a PFC.

Under the heat flux released on the plasma-facing tile surface, these components experience significant thermal stresses due to the material properties mismatch and thermal gradient between the heated surface and the cooling channel [23]; the highest stress concentration is at the bond interface [24].

The interfacial stresses responsible [25] for the structural integrity, which plays a key role in duplex joint structures, are the delamination (or peeling) and shear stresses; the first ones act normally to the interface, while the latter tangentially; from this point of view, the most critical domain is the free surface edge [26],[27]. What occurs in that place, is a stress singularity, where the thermal stresses reach an intensive peak; the intensification of stresses can generate interfacial debonding [22], which is the main failure mode characterizing these kinds of problems.

To better understand the thermo-mechanical issue in bi-material joint structures, both analytical and numerical points of view are investigated in the next paragraphs.

## **2.2 Review of analytical models of bi-material joint structures**

The interfacial stresses in bi-material joint structures have been the subject of matter for years, and several analytical models have been proposed. All the analytical models are based on the elementary beam theory [28], providing simplified formulations for the interfacial stresses according to different assumptions, as in the examples reported below. The existing analytical methods [29] predict the general character of the interfacial stresses, showing they are negligible in the bulk region and indicating the presence of the stress singularity at the free surface edge. That region is analyzed with a different analytical approach. In this scenario, numerical analyses are required.

### **2.2.1 Interfacial stresses analytic prediction**

One of the most studied models has been proposed by Suhri, firstly obtaining [25] second-order differential equations, and later [30] sixth-order differential equations implementing the “normal interfacial compliance” for making peeling stresses satisfy the self-equilibrated condition.

Starting from Suhri's models, a new formulation [31] has been proposed by C.Q. Ru, decreasing the order of the differential equations to the second one and satisfying at the same time the interfacial peeling stresses self-equilibrium, the zero-longitudinal force, and the zero-shear stress boundary conditions at the free edge. The introduced boundary conditions are reported in Eq. (1).

The basic assumption is the longitudinal interfacial displacement at a point depends not only on the interfacial shear stresses, as prescribed by Suhri, but also on the second gradient of the interfacial shear stresses at that point.

A bi-material elastic beam, as reported in **Figure 7**:

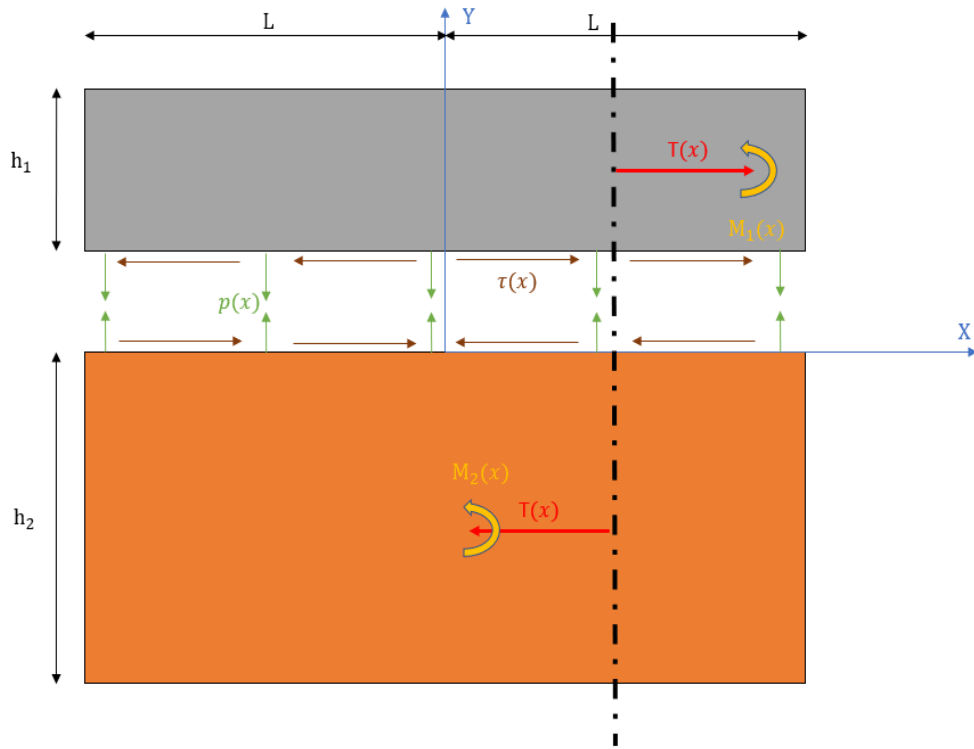


**Figure 7** Stress analysis model, where  $\tau(x)$  are the interfacial shear stresses,  $p(x)$  are the interfacial peeling stresses along the  $x$ -direction,  $T(x)$  is the longitudinal shear force;  $M_{1,2}(x)$  are the bending moments.

$$\begin{cases} \tau(L) = 0 \\ T(L) = 0 \\ \sum M(L) = 0 \end{cases} \quad (1)$$

The previously described boundary conditions lead to a closing solution for the analytical formulations of peeling and shear stresses. In the current study, those formulations are omitted, while the obtained behaviors are presented in **Figure 8** and **Figure 9**, based on a case study validated through the comparison to Eischen's model [32]. More details can be found in [31].

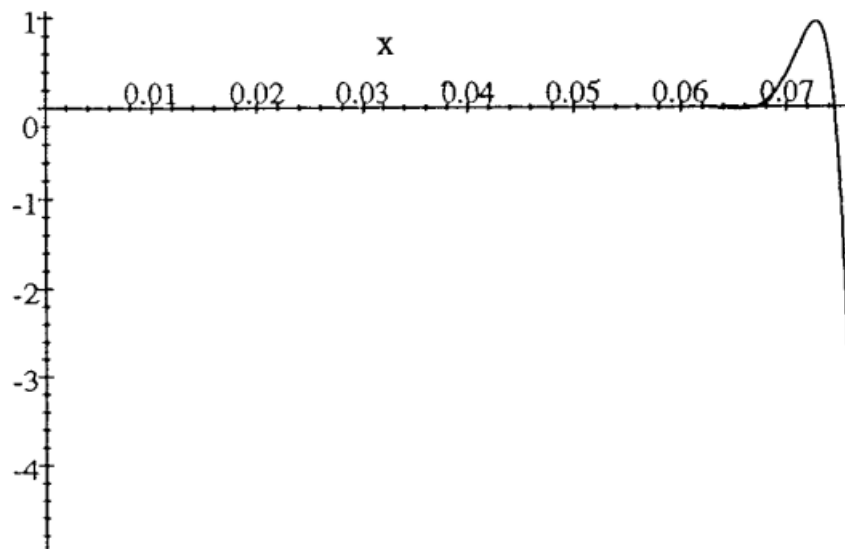


**Figure 8** Peeling stresses (MPa) obtained for a Silicon/Aluminium system, taken from [31].

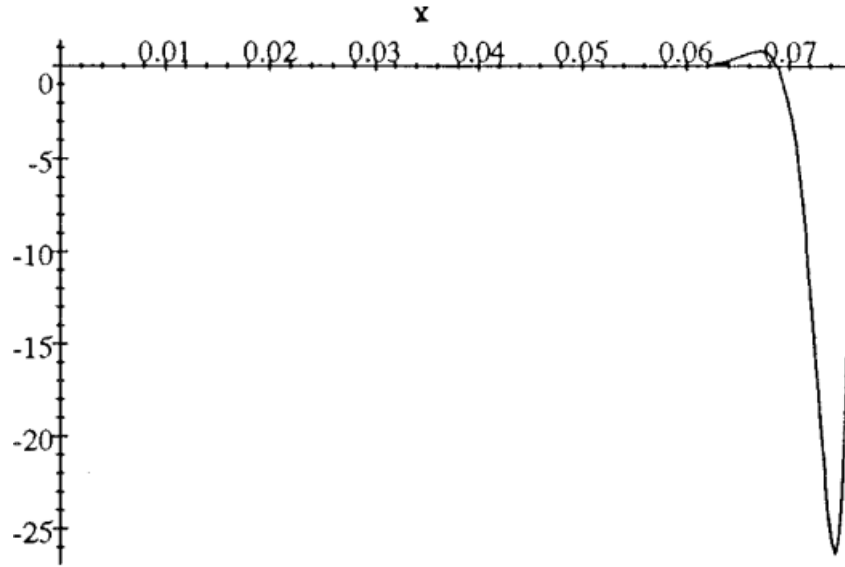


**Figure 9** Shearing stresses (MPa) obtained for a Silicon/Aluminum system, taken from [31].

### 2.2.2 The singularity at the free surface edge

In bonded joints characterized by two homogeneous and isotropic materials with different elastic properties, the stress state near the free edge is described by the Eq. (2) [33]:

$$\sigma_{ij}(r, \theta) = \frac{K}{(r/D)^\omega} f_{ij}(\theta) + \sigma_0 f_{ij0}(\theta) \quad (2)$$

where  $r$  and  $\theta$  are the polar coordinates and  $D$  is the characteristic dimension, such as the length  $L$ . That formulation is valid for rectangular geometries where  $\theta = 90^\circ$ , as the case of PFC where one material is the plasma-facing material (PFM) and the other one is the structural material for the HSS; a schematic configuration is shown in **Figure 10**.

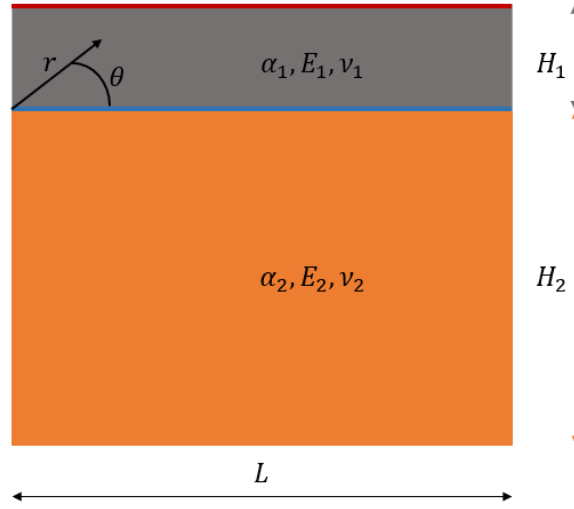


**Figure 10** General configuration of a duplex bond joint of a PFC at the free edge.

The other parameters are the stress intensity factor  $K$ , the regular stress term  $\sigma_0$ , which are proportional to the incremental temperature  $\Delta T$  and to the (thermal expansion coefficient) CTEs mismatch; the exponent of singularity  $\omega$ , the angular functions  $f_{ij}$  and  $\sigma_0$  are evaluated by analytical methods. Generally, all the introduced parameters depend on Young's modulus  $E$  and the Poisson coefficient  $\nu$ . This method has been developed in case of uniform temperature distribution, but later broadened to non-linear temperature profile, too; more details on the coefficient's formulations can be found in [34].

The introduced analytical method, as reported in [22], has been applied to different material configurations, typically used for PFCs, to evaluate the stress concentration at the free surface edge; the thermal stresses are only determined by the  $\Delta T$ . It has been confirmed for all the components the stress singularity is concentrated at the free surface edge; furthermore, the magnitude and the sign of the singularity are highly dependent on the degree of elastic constants and thermal expansion coefficient mismatch.

The tungsten-copper combination shows one of the most intensive singularities. As reported in the **Figure 11**, the singularity is tensile (positive peak) since  $\Delta T = -1 \text{ K} < 0$ . In case of  $\Delta T > 0$ , the singularity is compressive (negative peak).

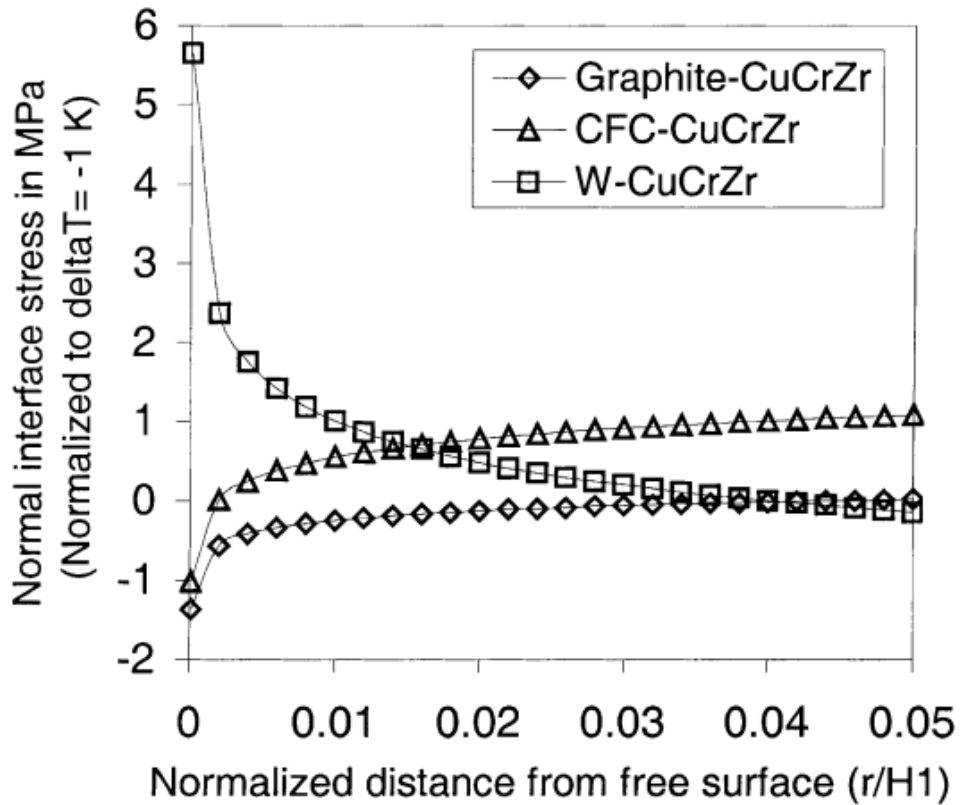


**Figure 11** Interfacial normal stresses near the free surface edge obtained analytically for different material combinations, taken from [22].

### 2.3 Numerical Models Review

Finite element analyses have been largely applied for bond structure modeling to validate the several analytic models proposed. Compared to analytical models, Pionke and Wempner showed FEM predicts the same interfacial stress behavior far from the free surface edge, where stresses are close to zero, and confirms that higher stresses are localized in a small region near the edge [29].

The FEM analysis shows convergence to the analytic methods only far from the free edge. Indeed, at the free edge, the interfacial stresses are highly dependent on the mesh size applied [35], reaching larger values while the mesh size is decreasing.

The comparison to FEM stress analysis using commercial software as ANSYS, confirms the same prediction, too. Its results have been compared with a

novel analytical model [36], developed by Xiang-Fa Wu and validated through other well-known analytical models, showing a good fitting of the interfacial stresses except at the free edge where they increase rapidly with the decrease of the mesh size.

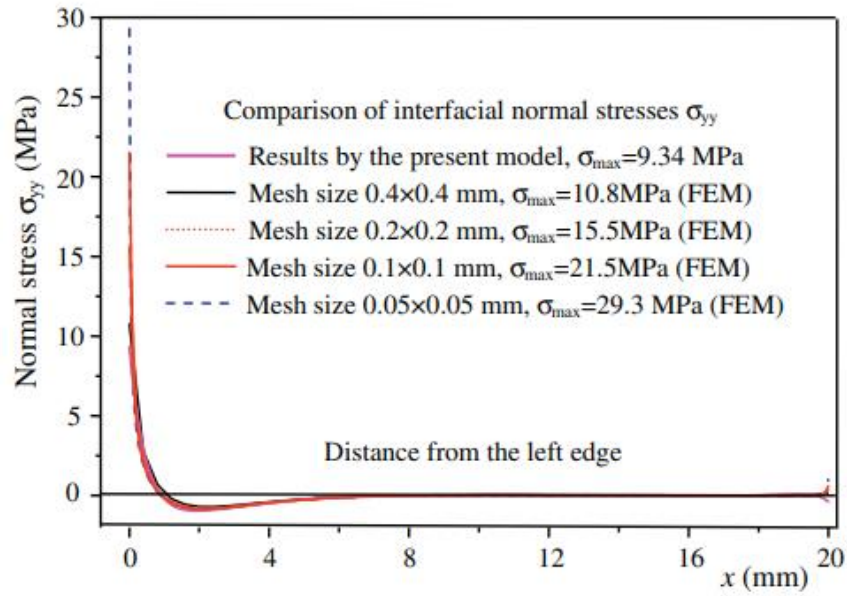


**Figure 12** Comparison of interfacial normal stresses predicted by an analytical method with those by FEM, taken from [36].

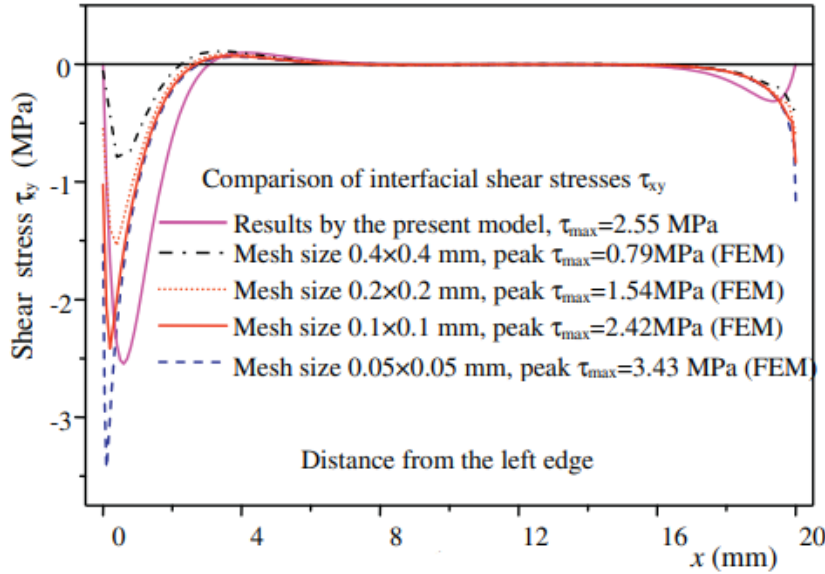


**Figure 13** Comparison of interfacial shear stresses predicted by an analytical method with those by FEM, taken from [36].

Considering **Figure 12**, it's clear that delamination peak is highest at the minimum mesh size applied. **Figure 13** demonstrates how the analytical method enforces the zero-shear stresses boundary condition at the free edge, which can only be achieved with a larger mesh size. When the mesh size is reduced, the shear stresses at the free edge are even further from reaching the zero-shear stress condition and the peak in shear stresses results increased.

## 2.4 A relevant case study: thermo-mechanical simulation of a simple array

In this paragraph, a typical PFC is analyzed by 3D finite element stress analysis, and the results are compared to what has been described in the previous paragraphs; in particular, the PFC modeled, is characterized by the same layer structure of the tile object of this work. The analyses are performed in STAR-CCM+ enabling the Stress Solid solver [37].

### 2.4.1 Geometry and Material properties

An equivalent model of a single array of the tile, as described in detail in section 1.2, is introduced; the current model is free of the micro-channels configuration in

the HSS and for this reason, is named “simple array”. A schematic view is reported in **Figure 14**:

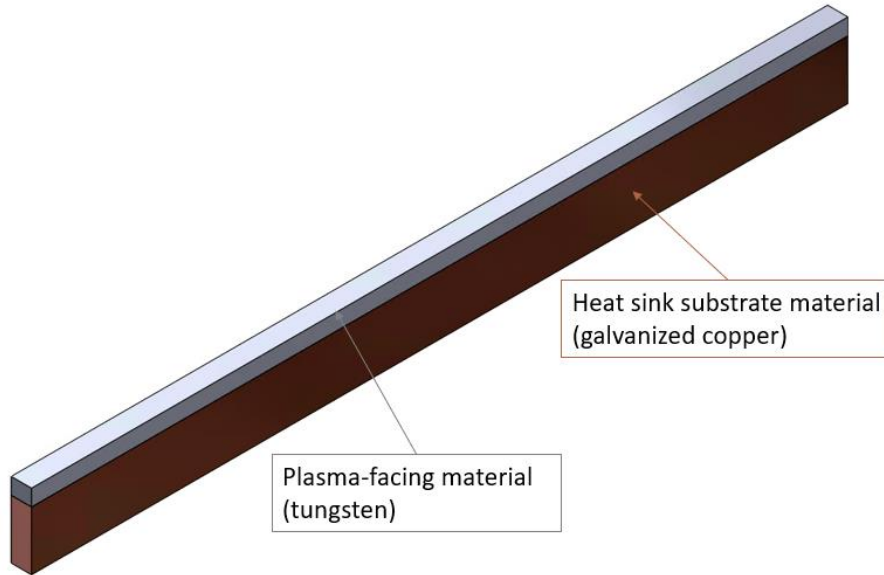


**Figure 14** Schematic 3D view of the simple array.

The thermo-mechanical properties of tungsten [38] and galvanized copper [20] used in the following analyses are reported in **Table 1**; the two materials are considered isotropic linear elastic materials.

**Table 1** Thermo-mechanical properties of tungsten and galvanized copper.

|                                  | <b>Tungsten</b>     | <b>Galvanized copper</b> |
|----------------------------------|---------------------|--------------------------|
| <b>E (GPa)</b>                   | 400                 | 110                      |
| <b><math>\alpha</math> (1/K)</b> | $4.4 \cdot 10^{-6}$ | $16.9 \cdot 10^{-6}$     |
| <b><math>\nu</math> (-)</b>      | 0.29                | 0.33                     |

The Young’s Modulus and the thermal expansion coefficient are dependent on the temperature; the values used in this work are constant since in the

temperature range considered, they don't change significantly and don't influence the results. The Poisson coefficient used is referred to elastic calculations.

## 2.4.2 Constraints and Temperature Load

The simple array is considered part of the tile, and the constraints are applied to account for the similarity to reality, simulating the free surface edges. In dealing with thermal stresses, constraints must be as realistic as possible to avoid local stress concentration. The following boundary conditions are applied, as reported in **Figure 15**:

- Zero normal displacement is applied to two array surfaces in contact with other arrays in the tile;
- One node is fixed in the three directions to totally constrain the model without being too restrictive;
- The other surfaces are free of any constraints;
- The interface between the PFM and the HSS is a mapped contact interface and the mechanical interaction between the two solid is bonded.

The simple array is subjected to a uniform temperature load of 350 K.

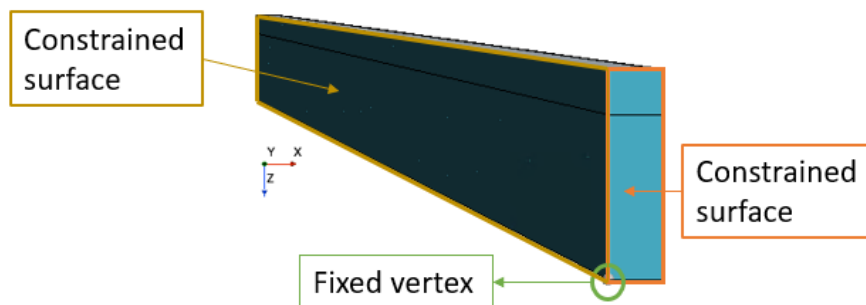


**Figure 15** Constraints applied to the simple array; all the other surfaces or nodes are free of any constraints.

### 2.4.3 Mesh

The mesh is generated using tetrahedral elements adding the mid-side nodes; in this way, quadratic tet10 elements are used to improve the accuracy of the results. The mesh base size<sup>5</sup> used in this case is 0.5 mm.

As discussed in section 2.3, a high mesh dependency at the free surface edge of the bond interface is expected; in the scope of investigating that in detail, mesh refinement is applied in the interested region, as highlighted in the

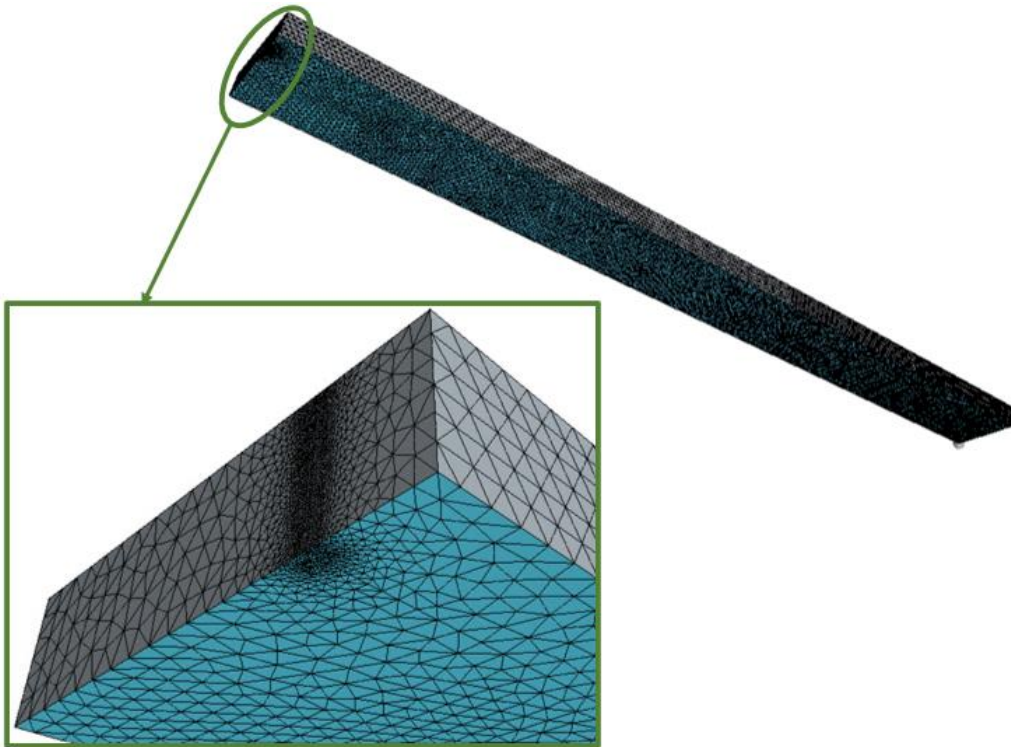


**Figure 16** Tetrahedral mesh generated on the simple array with a mesh refinement zoom applied on the free surface edge of the bond interface.

### 2.4.4 Simulation Results and Discussion

The results are analyzed in terms of stress evaluation at the bond interface, reported in **Figure 17**.

---

<sup>5</sup> The mesh base size is the characteristics length scale representing the size of the smallest feature of interest in the simulation geometry.

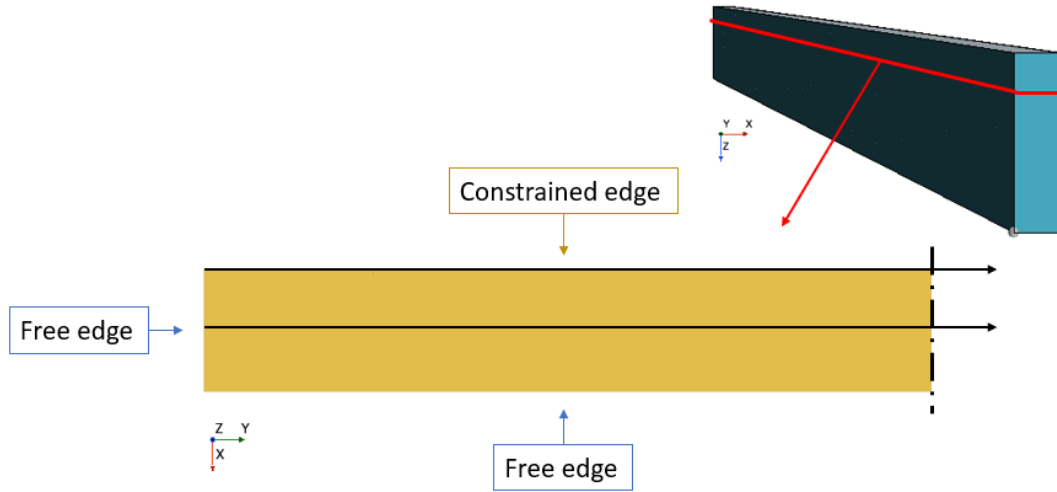


**Figure 17** Simple array with a zoom on the bond interface; peeling stresses are extracted along the line closer to the constrained edge while shear stresses are extracted along the central line.

The stress at any point is defined by the stress tensor in Eq. (3), where the diagonal terms are the normal stresses, while the off-diagonal terms are the shear stresses:

$$\bar{\sigma} = \begin{bmatrix} \sigma_{ii} & \sigma_{ij} & \sigma_{ik} \\ \sigma_{ji} & \sigma_{jj} & \sigma_{jk} \\ \sigma_{ki} & \sigma_{kj} & \sigma_{kk} \end{bmatrix} \quad (3)$$

The indexes  $i, j, k$  correspond respectively to the  $x, y, z$  axes. In this case, the components of the stress tensor analyzed are:

- $\sigma_{kk}$ , which is the normal stress component normal to the bond interface and corresponding to the interfacial delamination or peeling stress;
- $\sigma_{jk}$ , which is the shear stress component corresponding to the interfacial shear stress.

The stress distribution is analyzed and graphed along a line that measures the distance from the free surface edge, where  $y = 0$ . This direction is selected because it allows stresses to fully develop along the longer path. To avoid the influence of the opposite free edge in the case of peeling stresses, the line is situated closer to the constrained edge. On the other hand, in the case of shear stresses, the line is placed centrally to the bond interface, as depicted in **Figure 17**.

The delamination or peeling stresses are plotted in **Figure 18**. A mesh refinement at the free edge is applied and as expected, the delamination peak reaches higher values decreasing the mesh base size. The delamination peak is compressive since the thermal load applied is positive.

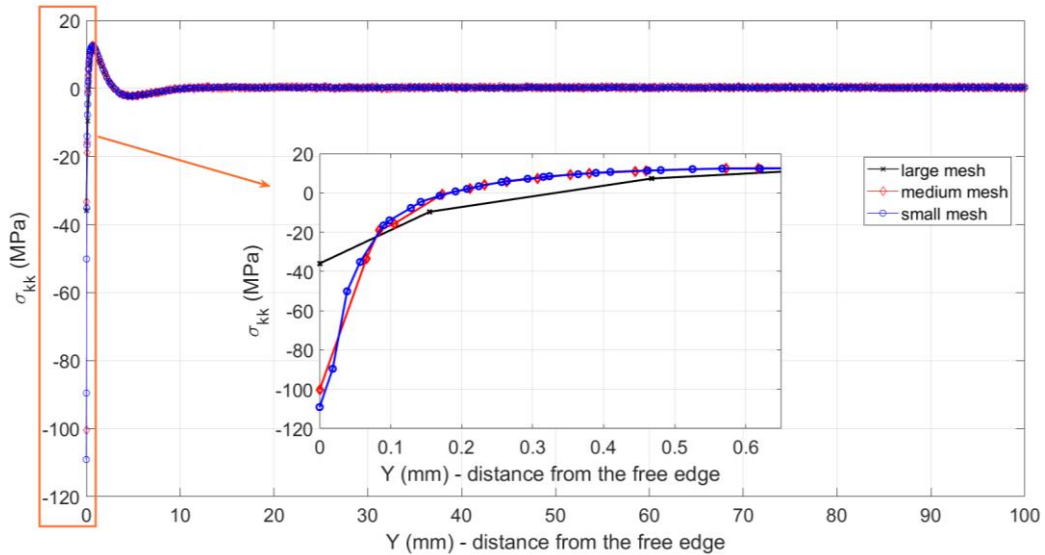


**Figure 18** Delamination or peeling stresses along a line on the bond interface (simple array); a focus on the delamination peak increasing with the mesh base size decreasing is reported.

The shear stresses are plotted in **Figure 19**; also in this case, as previously discussed, the zero-boundary condition is “almost” reached by the large mesh and not exactly because of the numerical approach; furthermore, the shear stress peak, as expected, increases decreasing the mesh base size.

It’s clear from both the plots, the difference of stress peaks in the case of the medium (0.09 mm) and the small (0.05 mm) mesh base sizes applied is so lower than the large one (0.5 mm); that reveals a convergence with the mesh refinement, even if it cannot be completely reached, as shown on page 14.

For this reason, the medium mesh base size is chosen for further evaluations, in order to find a balance with the computational cost, particularly high because of the use of the mid-side nodes. The implementation of the mid-side nodes is visible from the previous plots where the number of values agrees with the number of nodes used in the modeling.

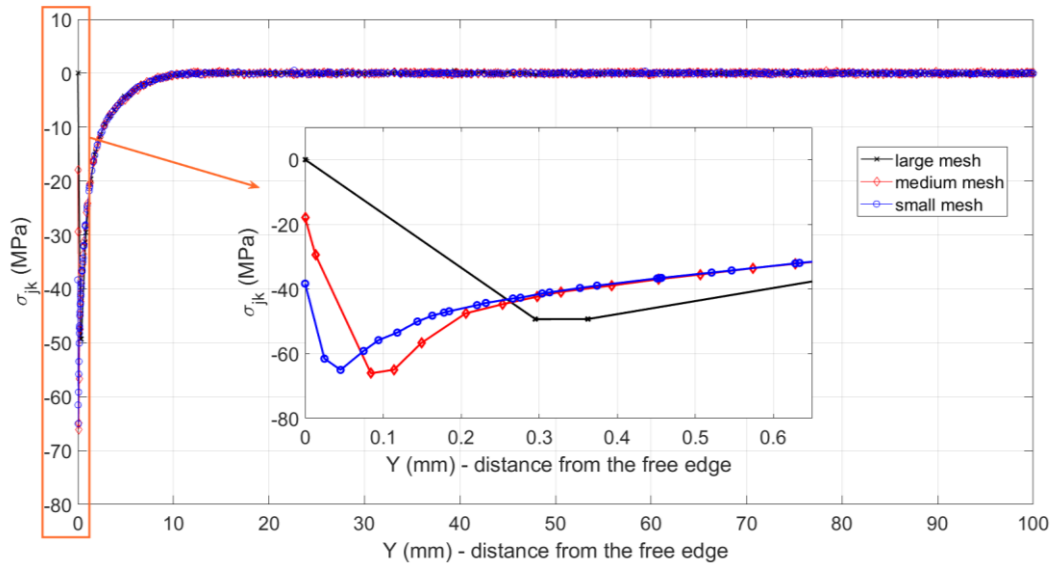


**Figure 19** Shear stresses along a line on the bond interface (simple array); a focus on the zero-boundary condition and the shear stress peak increasing with the mesh base size decreasing is reported.

## Chapter 3

# The thermo-mechanical modeling of a tile array

### 3.1 From the tile to the single array

To reduce the computational cost of the thermo-mechanical modeling of the entire tile introduced in section 1.2, a single array is taken into consideration for the stress evaluation. In particular, the single array is equipped with a half inlet and half outlet manifold, considering the symmetry of the structure.

The single array approach is applied to both the MCs and PS configuration; the dimensions of the two models are identical. In the first step, a thermo-mechanical comparison is conducted by subjecting both models to a uniform specified temperature. This aims to compare the results to those obtained from the simple array. In the second step, the interfacial stresses between the MCs and PS arrays are compared by applying the temperature map generated by the respective thermal-hydraulic simulation.

### 3.2 Tile array equipped with MCs

#### 3.2.1 Geometry and material properties

The MCs-array is equipped with 120 MCs and the geometry is reported in **Figure 20** and **Figure 21**; the material properties are the same used for the simple array (**Table 1**).

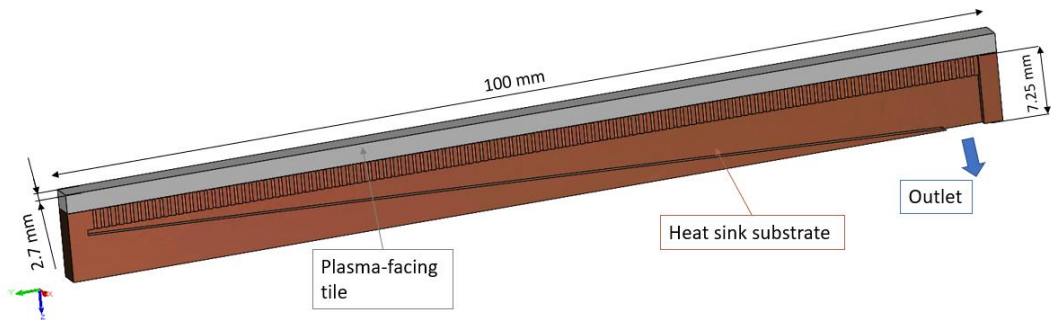


**Figure 20** Schematic 3D view of MCs-array (outlet manifold view).

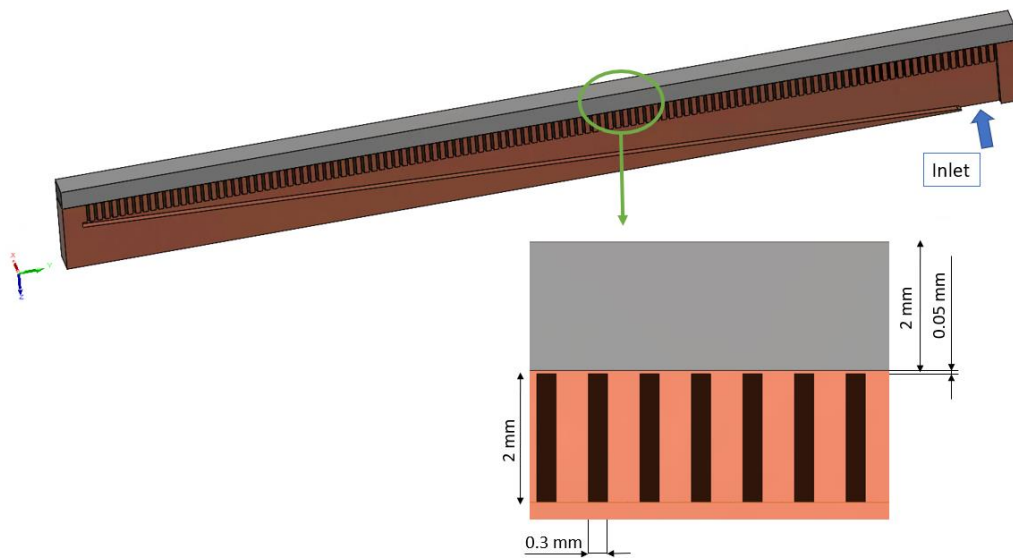


**Figure 21** Schematic 3D view of MCs-array (inlet manifold view) with a zoom on the MCs structure.

### 3.2.2 Constraints and Temperature Load

The MCs-array is constrained in the same way described in section 2.4.2; the uniform specified temperature is also the same (350 K).

### 3.2.3 Mesh

The mesh generated is tetrahedral and the mid-side nodes are applied; the mesh base size is 0.5 mm. In this case, two mesh refinements are implemented:

1. One refinement is driven by the need of accurately accounting for the thickness between the MCs and the bond interface, as visible in **Figure 22**; this refinement is named “Thickness mesh refinement”;
2. The other refinement is due to consider the free surface edge, as previously introduced for the simple array (page 19); this refinement is named “Free edge mesh refinement”.

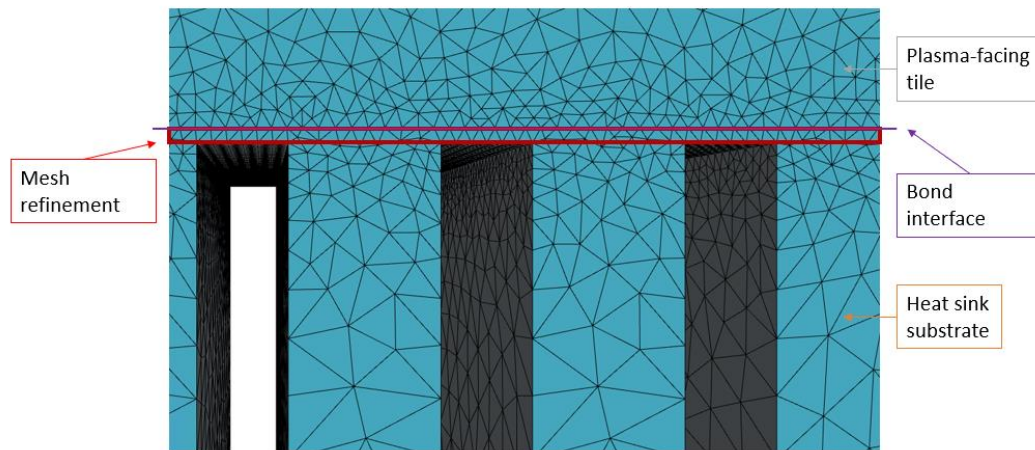


**Figure 22** Mesh refinement applied on the thickness between the bond interface and the MCs.

## 3.2.4 Simulation Results and Discussion

### 3.2.4.1 Thickness mesh refinement

The stress evaluation is conducted as previously done for the simple array (section 2.4.4). Firstly, only the thickness mesh refinement is adopted with the application of three different mesh base sizes to check the mesh independency.

The MCs-array is characterized by stress fluctuations along the line in correspondence of the MCs. In that region, the stresses should be zero, as indicated by literature and the simple array approach. However, this is not the case because the MCs are located too close to the bond interface and thus affect the behavior of interfacial stresses.

Three mesh base sizes applied are compared in terms of interfacial stresses median, delamination peak, and zero-shear condition value. The characteristic size of the different mesh is calculated as  $\sqrt[3]{V/N}$ , where V is the refinement volume and N is the element number inside. The median<sup>6</sup> is chosen as the statistics index because the interest is to quantify the central tendency of fluctuations; the presence of some extreme values in the distribution makes the median the most appropriate index.

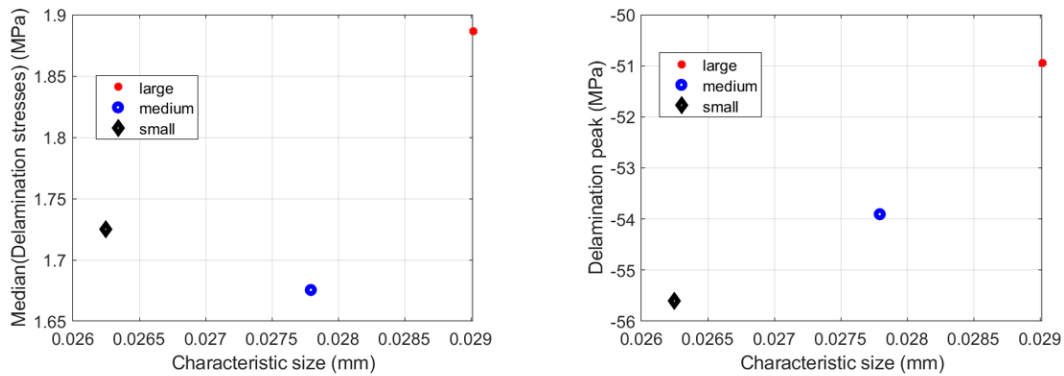


**Figure 23** Thickness mesh refinement (MCs-array), delamination stresses comparison: median (on the left) and delamination peak (on the right).

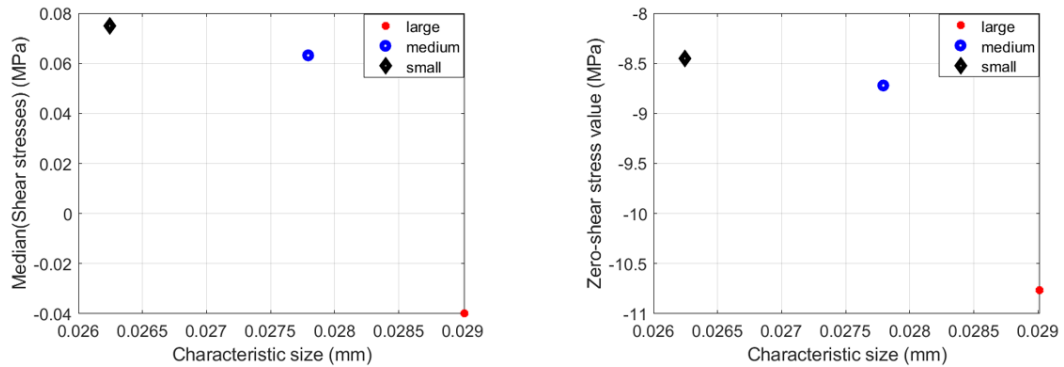


**Figure 24** Thickness mesh refinement (MCs-array), shear stresses comparison: median (on the left) and zero-shear stress value (on the right).

<sup>6</sup> The median is a measure of central tendency that represents the value separating the upper half of dataset from the lower half.

The large and medium mesh base sizes are characterized by a difference inferior compared to the difference between the medium and the small ones; in addition, it's clear from **Figure 23** and **Figure 24** the difference of the plotted values between the medium and the small mesh base sizes becomes negligible in comparison with the difference between the large and medium ones. For this reason, the medium mesh size is chosen for further evaluations, accounting for the computational cost, too. **Figure 25** and **Figure 26** show the typical interfacial stress behavior in the case of the MCs-array, implementing the medium-thickness mesh refinement.

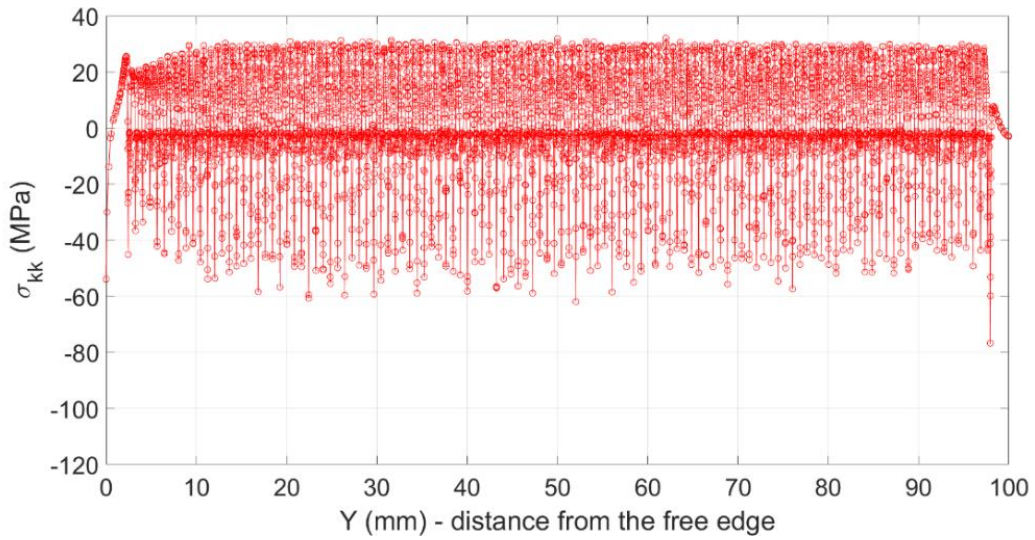


**Figure 25** Delamination or peeling stresses along a line on the bond interface (MCs-array); thickness mesh refinement applied only.

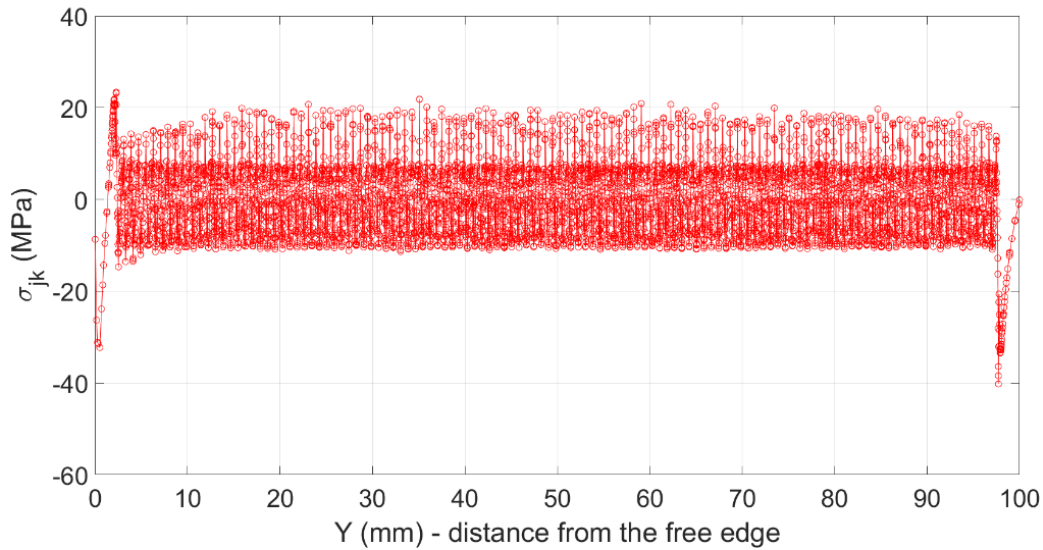


**Figure 26** Shear stresses along a line on the bond interface (MCs-array); thickness mesh refinement applied only.

### 3.2.4.2 Free edge mesh refinement

Once the thickness mesh refinement is implemented with the mesh base size chosen in the previous paragraph, the free edge mesh refinement is also implemented. The scope is to compare the interfacial stresses of the different models at the free edge; since the stresses in that region are high mesh dependent, the free edge mesh refinement with the same values of mesh base size is necessary.

For this reason, the mesh base size at the free edge chosen in the simple array (section 2.4.4), is implemented; the interfacial stresses, at the free edge, in the case with the mesh refinement and without are compared. As expected, the MCs-array shows the same effects obtained and discussed for the simple array.

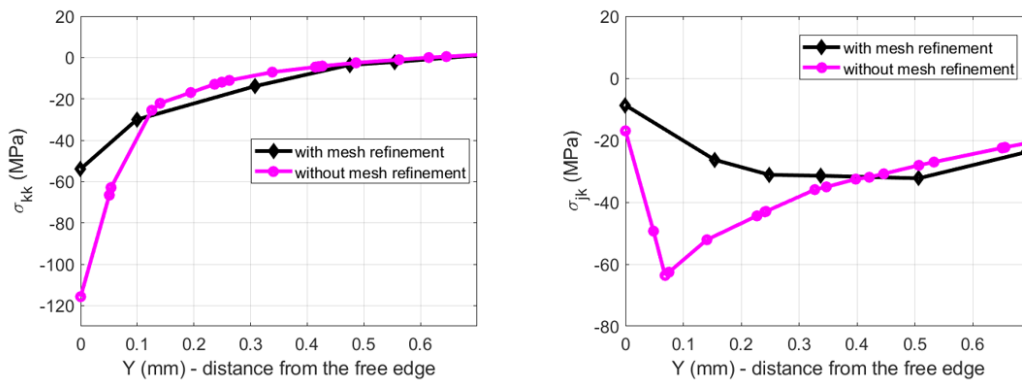


**Figure 27** MCs-array, delamination or peeling (on the left) and shear (on the right) stress: zoom on the free surface edge region highlighting the mesh refinement effect.

### 3.3 Tile array equipped with PS

#### 3.3.1 Geometry and material properties

The PS-array is equipped with 20 Porous blocks; the dimensions are reported in **Figure 28** and the material properties are the same as the simple and MCs arrays, reported in **Table 1**.

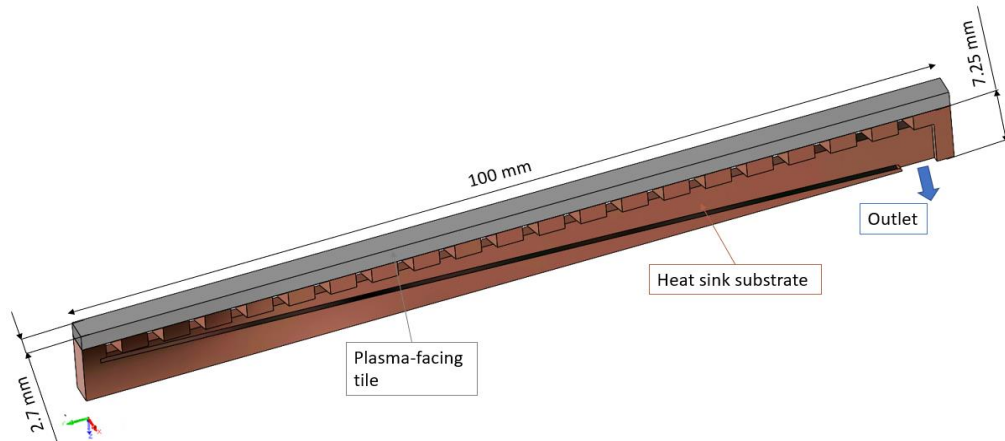


**Figure 28** Schematic 3D view PS-array (outlet manifold view).

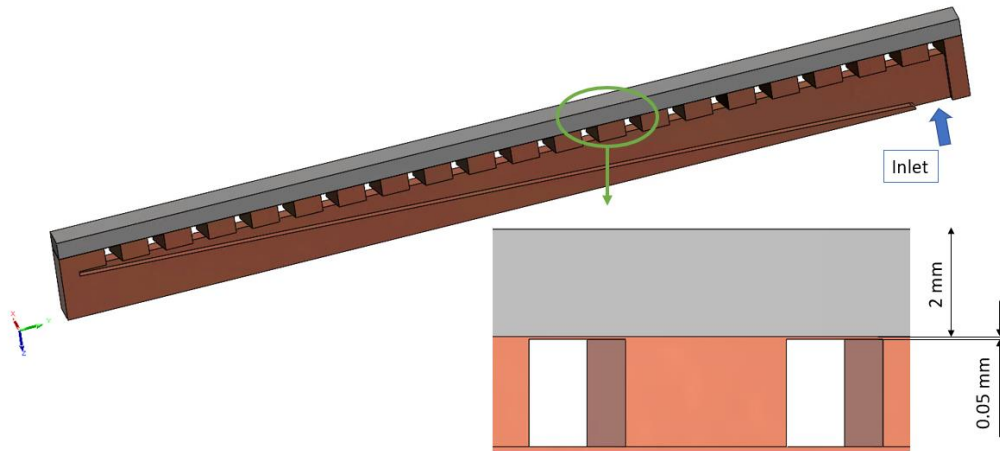


**Figure 29** Schematic 3D view PS-array (inlet manifold view) with a zoom on the PS blocks structure.

### 3.3.2 Constraints and Temperature Load

The PS-array is constrained in the same way described on page 18; the thermal load applied is uniform with a magnitude of 350 K.

### 3.3.3 Mesh

The mesh generated is tetrahedral and the mid-side nodes are applied; the mesh base size is 0.5 mm. The two mesh refinements introduced in the MCs-array on section 3.2.3 are implemented:

1. Thickness mesh refinement, using the mesh base size chosen on page 25;
2. Free edge mesh refinement, using the mesh base size chosen on page 19.

### 3.3.4 Simulation Results and Discussion

The interfacial stresses are extracted as in all the previous analyses and reported in **Figure 30** and **Figure 31**. As in the MCs-array, the PS-array is characterized by stress fluctuations due to the presence of the PS blocks very close to the bond interface.

In particular, the presence of high-stress peaks along the bond interface, suggests the thickness between the bond interface and the block (channel) should be increased to avoid the possibility of the interface debonding. This point is discussed in detail in section 3.5.

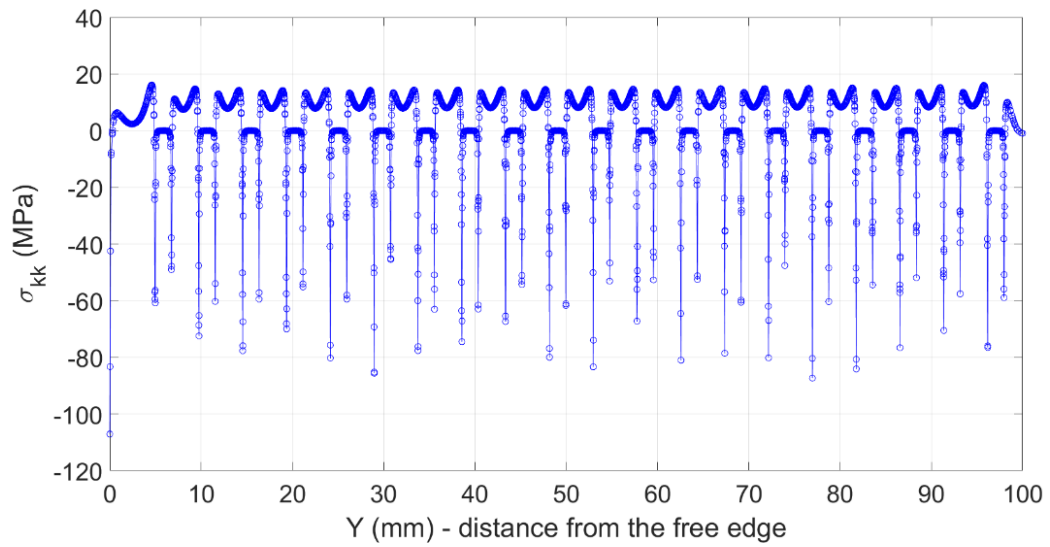


**Figure 30** Delamination or peeling stresses along a line on the bond interface (PS-array).

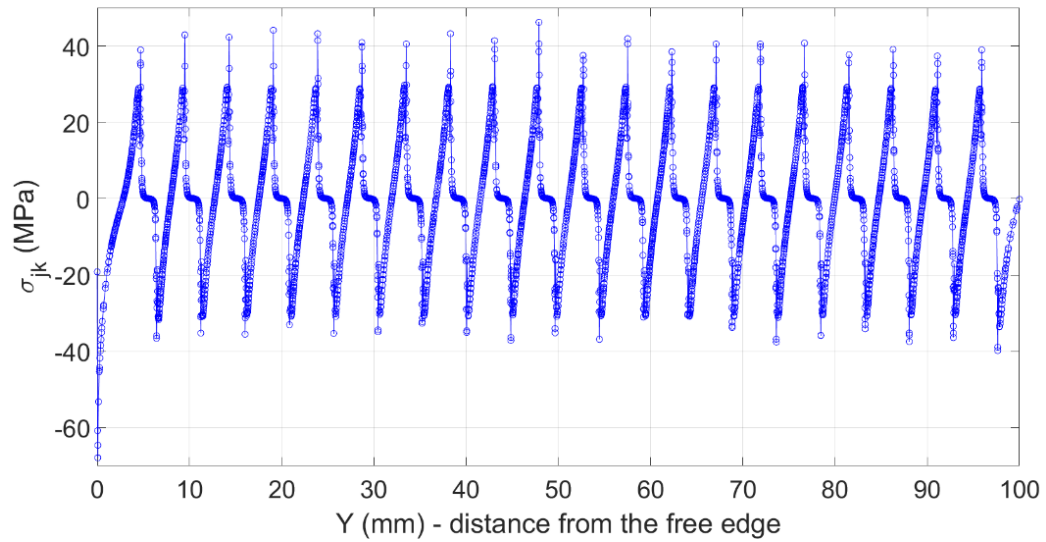


**Figure 31** Shear stresses along a line on the bond interface (PS-array).

### 3.4 Discussion on Models comparison

The models introduced are now compared. In particular, the comparison is in terms of interfacial stresses at the free edge, being, as previously discussed, the most critical domain for structural integrity.

The simple, MCs and PS arrays are compared by applying the same uniform specified temperature of 350 K. The MCs-array and PS-array are also compared by applying the temperature map extracted from the thermal-hydraulic simulations.

#### 3.4.1 Uniform specified temperature

The three models are compared as described. They predict very similar interfacial stresses at the free edge, in particular for the shear stresses.

The MCs-Array is characterized by the highest delamination peak; that's reasonable since the micro-channels shape is rectangular with 90° corners. In addition, the MCs are highly repeated along the bond interface leading to an intensification of the stresses.

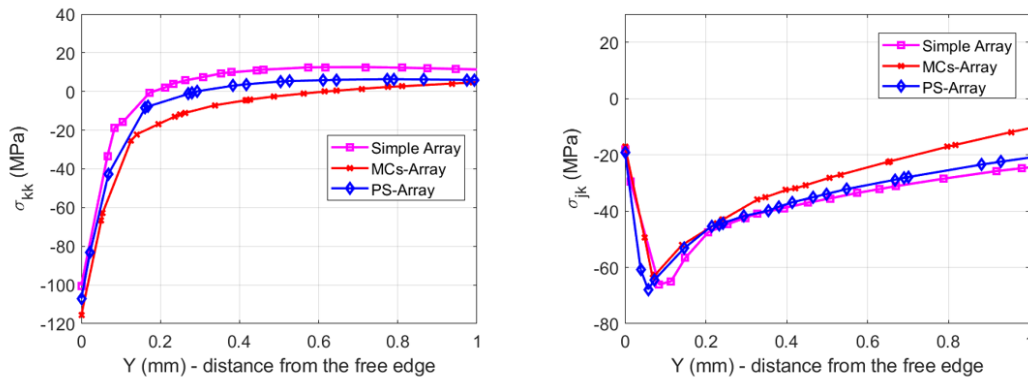


**Figure 32** Delamination or peeling (on the left) and shear (on the right) stress: zoom on the free surface edge region comparing the simple, MCs and PS arrays with a uniform temperature load applied.

#### 3.4.2 Temperature maps

The thermo-hydraulic simulation is set for the MCs-array and the PS-array; the model setup is discussed in section 4.5.1. In this case, the boundary conditions are *inlet mass flow rate* = 29 g/s and a uniform *heat flux* = 5 MW/m<sup>2</sup> on the

tungsten surface. Those boundary conditions are applied according to the operational constraints of the GLADIS facility at the IPP and implemented for the thermo-hydraulic validation of the PS-model [13], as briefly discussed in section 1.3.

The temperature maps are extracted from the finite volume mesh used in thermo-hydraulic analyses and imported on the finite element mesh used for the thermo-mechanical analyses, as temperature load.

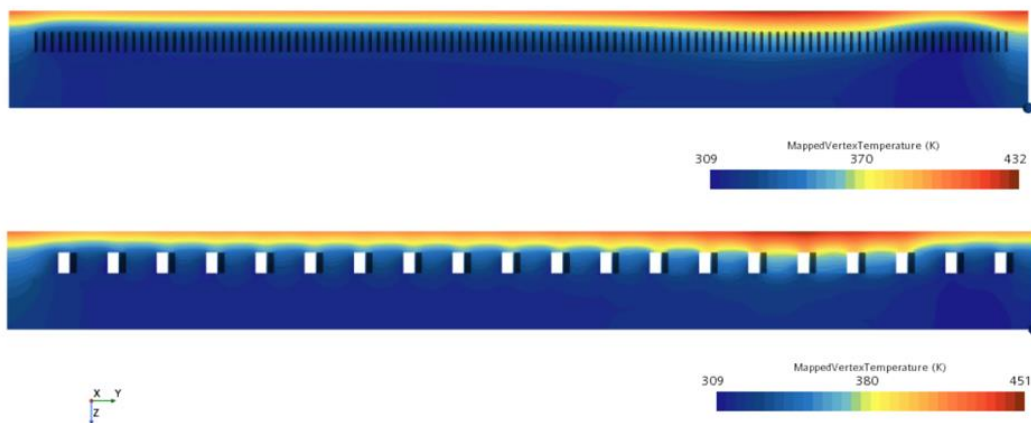


**Figure 33** Temperature maps applied on the MCs-array (top figure) and on the PS-array (bottom figure) as thermal load.

In this case, the PS-array overestimates the interfacial stresses in comparison with the MCs-array. This is completely reasonable since the PS-array overestimates also the temperature and this is reflected in the stress evaluation. In particular, the overestimation is evident for the delamination peak evaluation.

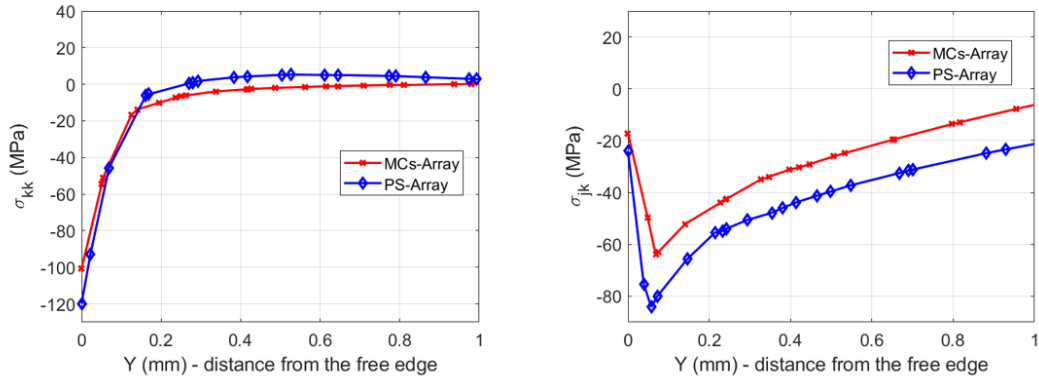


**Figure 34** Delamination or peeling (on the left) and shear (on the right) stress: zoom on the free surface edge region comparing the MCs and PS arrays with a temperature map applied.

### 3.5 Application of the lumped model

This section employs PS-array modeling to demonstrate the advantages of augmenting the thickness between the PS blocks (generally the water channels) and the bond interface. Specifically, the thickness is elevated from 0.05 mm, as depicted in **Figure 29**, to 0.5 mm and 1 mm. These thickness values are selected based on the improved manufacturing feasibility in an HSS composed of galvanized copper, as recommended by the manufacturing company.

Apart from the thickness increase, all other model configurations discussed in section 3.3 remain unchanged.

**Figure 35** and **Figure 36** illustrate a significant reduction in the peak values of interfacial stresses along the bond interface far from the free edge with an increase in the considered thickness. In particular, shear stresses (in case of thickness=1 mm) converge towards zero at a distance from the free edge, as predicted by simple array modeling and literature review.

Additionally, analytical models [36] support the finding that the delamination stress peak increases while the shear stress peak decreases as the thickness increases. However, the increase in the delamination peak is significantly less noticeable when compared to the reduction in the interfacial stress peak away from the free edge.

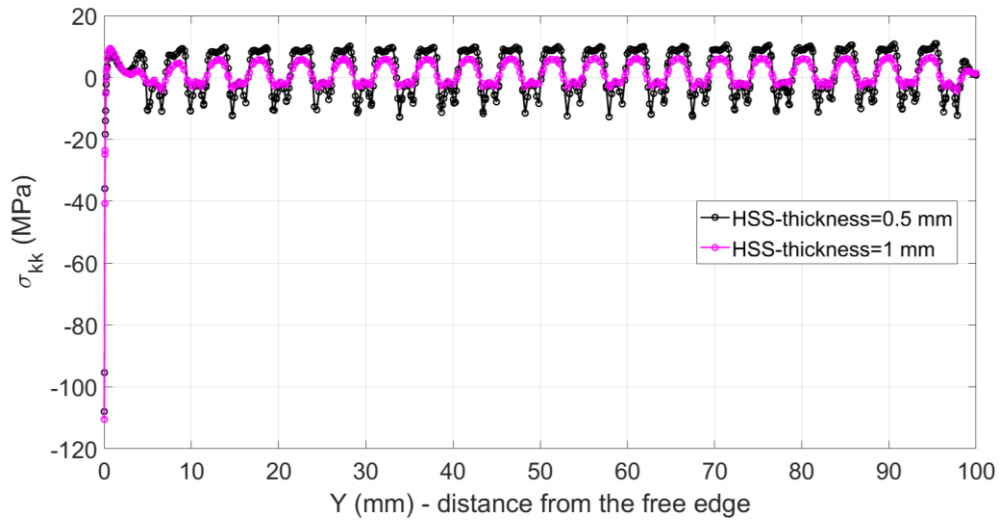


**Figure 35** Delamination or peeling stresses along a line on the bond interface (PS-array), with two thickness increases between the PS blocks and the bond interface.

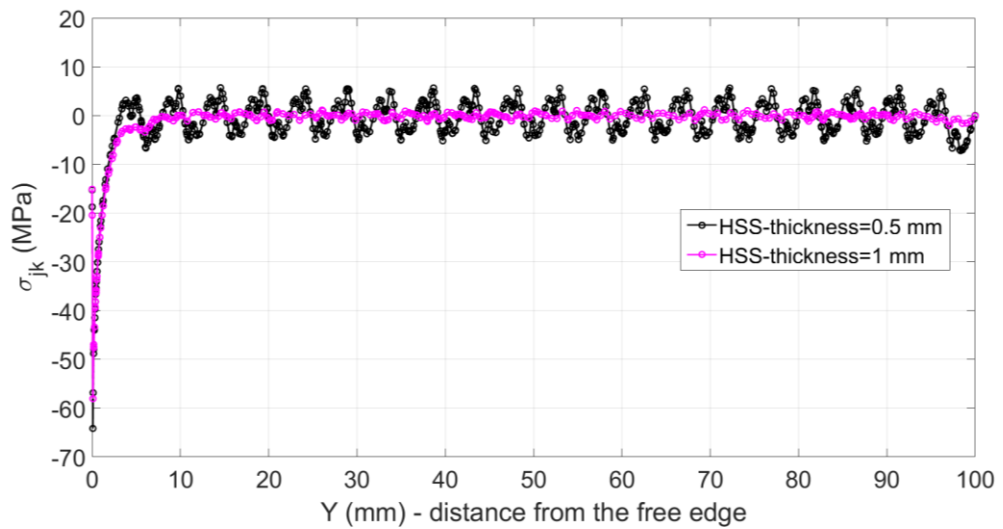


**Figure 36** Shear stresses along a line on the bond interface (PS-array), with two thickness increases between the PS blocks and the bond interface.

## Chapter 4

# MCs tiles connection in an entire divertor target module

In this section, the focus is on the second aim of the current study. Specifically, different configurations of the tiles connection in one target module (TM) are analyzed by implementing some improvements on the tile design and taking into consideration the operational constraints.

### 4.1 Tile design improvement

Considering the half tile, it has been demonstrated in Ref. [13] that the temperature hotspot is concentrated at the tile's edge due to the presence of uncooled solid in proximity to the last array of the tile. To reduce the risk of boiling at that point, the copper thickness is decreased from 3.4 mm, the initially designed value, to 1 mm, which is still acceptable for ensuring that the micro-channels can withstand the pressure drop. A representation is reported in **Figure 37**.

Taking also into account both the manufacturing process of galvanized copper and the concerns regarding interfacial stresses at the bond interface (as discussed in section 3.5), it has been deemed necessary to increase the thickness between the MCs and the bond interface from 0.05 mm to 1 mm, as depicted in **Figure 38**.

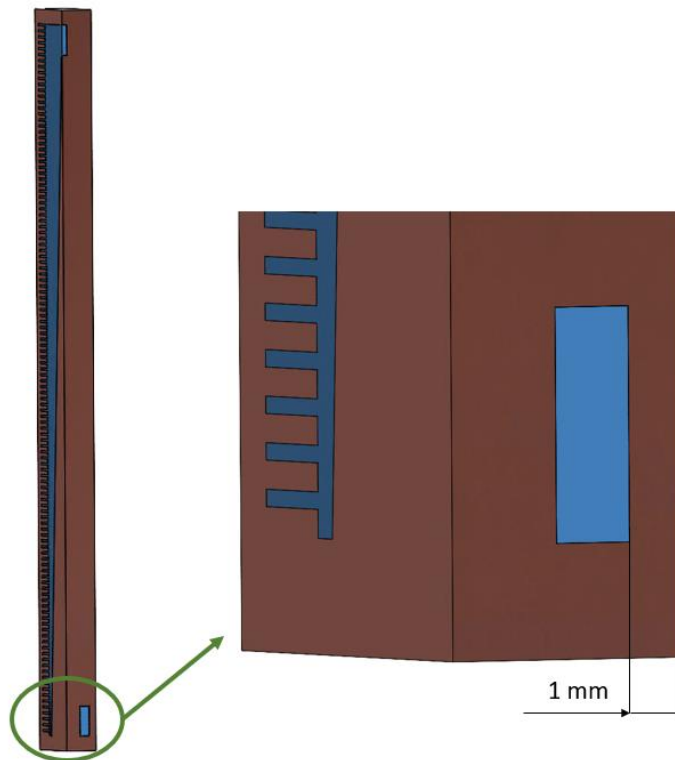


**Figure 37** Last tile array, with the manifold inlet and outlet cut; a zoom of the new HSS thickness is reported, in respect of the distance from the outlet section.

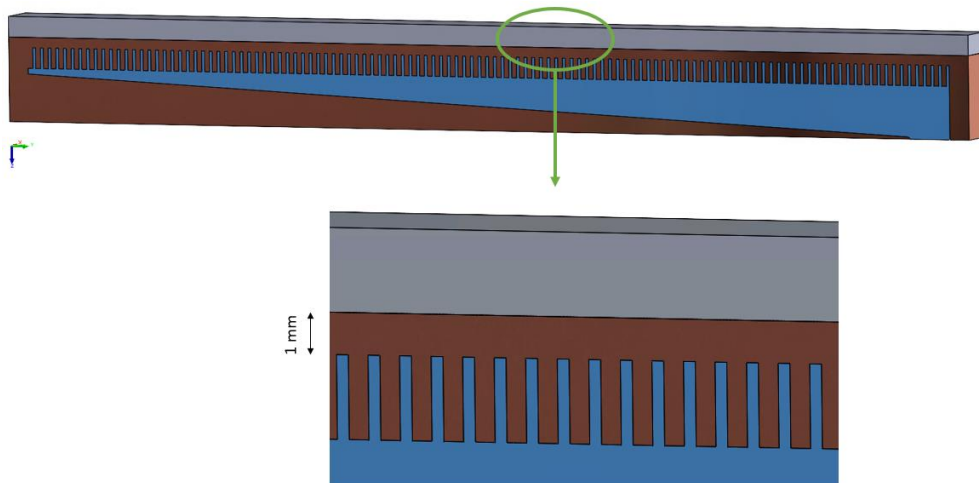


**Figure 38** Tile array with a zoom on the new thickness between MCs and bond interface.

## 4.2 Operational constraints

The proposed TM configurations are based on the respect of the following operational constraints:

- Single-phase flow
- $\text{Pressure}_{\text{inlet}} = 25 \text{ bar}$ ,  $\text{Pressure}_{\text{outlet}} = 10 \text{ bar}$
- Pressure drop allowed = 15 bar
- One water pump available with an inlet mass flow rate ( $\text{mfr}_{\text{inlet}}$ ) = 5 kg/s
- Heat flux<sub>main</sub> = 10 MW/m<sup>2</sup> - on a surface of 40 cm (toroidal) x 60 cm (poloidal)
- Heat flux<sub>max</sub> = 15 MW/m<sup>2</sup> - on a surface of 40 cm (toroidal) x 60 cm (poloidal)
- $\Delta T_{\text{increase,max}} \sim 50 \text{ K}$
- Surface available  $\sim 0.25 \text{ m}^2$

The most important constraints to absolutely respect are the single-phase flow and the pressure drop allowed; the first one is discussed in detail in paragraph 4.5.

The tiles can be connected either in series or parallel. When connected in series, mass flow rate conservation is ensured, while connecting them in parallel ensures pressure drop conservation, in accordance with electric similarity. Given the dimensions of each tile (10 cm x 10 cm) and the size of the TM, a maximum of 4 tiles can be connected in the toroidal direction, and up to 6 tiles can be connected in the poloidal direction.

## 4.3 Hydraulic simulation – PS half tile

Based on previous considerations, the maximum  $\text{mfr}_{\text{inlet}}$  is determined for a single tile that corresponds to an acceptable pressure drop for the entire TM connection. To achieve this, hydraulic simulations are conducted on a half-tile equipped with PS blocks (**Figure 39**), taking advantage of the great computational cost reduction.

The following models are used:

- 3D, steady state
- Turbulence Model K-Omega SST, with all  $y^+$  wall treatment

- Segregated flow
- Segregated fluid temperature.

The water properties are dependent on pressure and temperature.

The following initial conditions are imposed:

- Temperature of the water at the inlet: 27 °C
- Pressure at the outlet: 10 bar.

The following boundary conditions are imposed:

- Fluid inlet surface: inlet mass flow rate
- Fluid outlet surface: pressure outlet
- Manifold cut surface: symmetry plane.

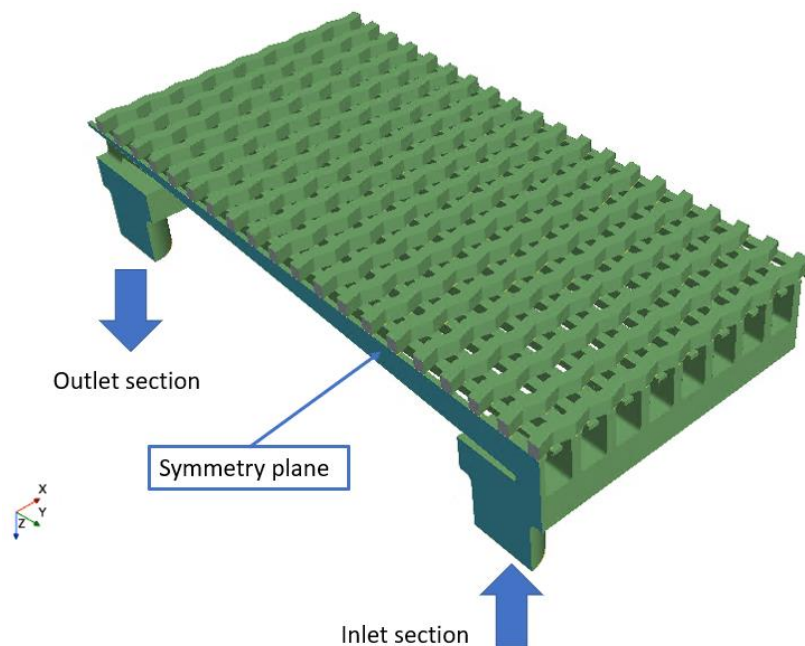


**Figure 39** Half-tile (only fluid) equipped with PS blocks.

The mesh implemented is polyhedral with 6 layers of prismatic cells on the manifold wall and avoiding the PS blocks. More details can be found in Ref. [13].

In the same reference can be found the porous coefficients found in the PS calibration and reported in **Table 2**.

**Table 2** Porous coefficients coming out from the PS calibration, taken from Ref. [13].

| Porosity | Porous inertial resistance (kg/m <sup>4</sup> ) | Porous viscous resistance (kg/m <sup>3</sup> s) | Horizontal thermal conductivity (W/mK) | Vertical thermal conductivity (W/mK) |
|----------|---|---|--|--------------------------------------|
| 0.5      | 7.04*10 <sup>5</sup>                            | 1.89*10 <sup>6</sup>                            | 4.6                                    | 59.8                                 |

The pressure drop is computed for different values of the inlet mass flow rate and the results are reported in the hydraulic characteristics (**Figure 40**). The computed pressure drops are used to evaluate the possible tiles connection in the TM checking the constraint of total pressure drop allowed.

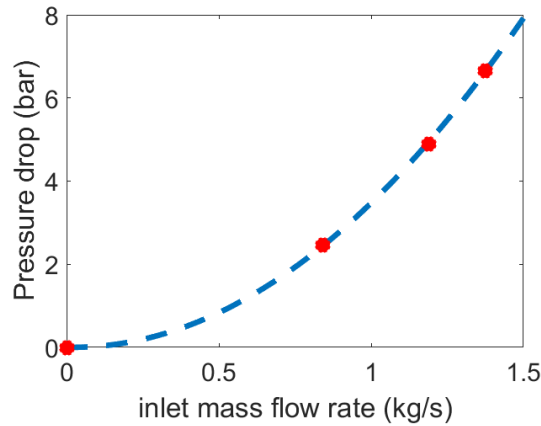


**Figure 40** Hydraulic characteristics computing the pressure drop for different inlet mass flow rate values on a half-tile equipped with PS blocks.

## 4.4 Tiles connection proposals

The tiles connection proposals are the following:

- **Proposal 1:** 6 parallel paths connecting 4 tiles in series (3 poloidally and 1 toroidally), **Figure 41**.

In this case, each tile is cooled by a  $mfr_{inlet}$  of 1.0 kg/s computing a pressure drop of 3.48 bar. The hydraulic connection leads to:

$$total\ mfr_{inlet} = 1.0 \frac{kg}{s} * 6 = 6.0 \frac{kg}{s}$$

$$\text{total pressure drop} = 3.48 \text{ bar} * 4 = 13.92 \text{ bar}$$

- **Proposal 2:** 4 parallel paths connecting 6 tiles in series (4 poloidally and 2 toroidally), **Figure 42.**

In this case, each tile is cooled by a  $mfr_{inlet}$  of 0.84 kg/s computing a pressure drop of 2.46 bar. The hydraulic connection leads to:

$$\text{total } mfr_{inlet} = 0.84 \frac{kg}{s} * 4 = 3.36 \frac{kg}{s}$$

$$\text{total pressure drop} = 2.46 \text{ bar} * 6 = 14.76 \text{ bar}$$

- **Proposal 3:** 8 parallel paths connecting 3 tiles in series poloidally, **Figure 43.**

In this case, each tile is cooled by a  $mfr_{inlet}$  of 1.19 kg/s computing a pressure drop of 4.9 bar. The hydraulic connection leads to:

$$\text{total } mfr_{inlet} = 1.19 \frac{kg}{s} * 8 = 9.52 \frac{kg}{s}$$

$$\text{total pressure drop} = 4.9 \text{ bar} * 3 = 14.7 \text{ bar}$$

- **Proposal 4:** 4 parallel paths connecting 6 tiles in series poloidally, **Figure 44.**

In this case, each tile is cooled by a  $mfr_{inlet}$  of 0.84 kg/s computing a pressure drop of 2.46 bar. The hydraulic connection leads to:

$$\text{total } mfr_{inlet} = 0.84 \frac{kg}{s} * 4 = 3.36 \frac{kg}{s}$$

$$\text{total pressure drop} = 2.46 \text{ bar} * 6 = 14.76 \text{ bar}$$

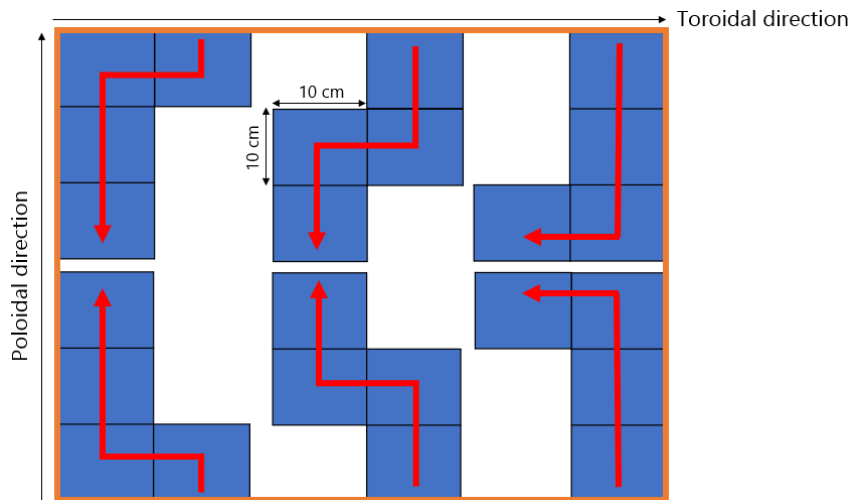


**Figure 41** Proposal 1: 6 parallel paths connecting 4 tiles in series (3 poloidally and 1 toroidally); each tile is represented by a blue block, while each parallel path is by a red arrow.

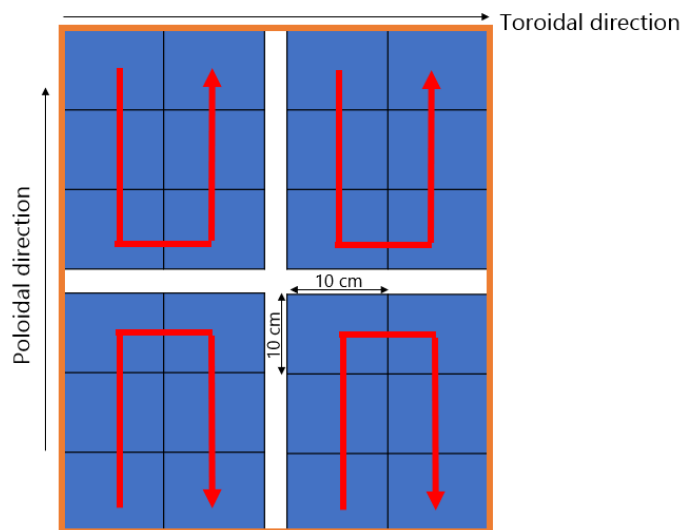


**Figure 42** Proposal 2: 4 parallel paths connecting 6 tiles in series (4 poloidally and 2 toroidally); each tile is represented by a blue block, while each parallel path is by a red arrow.

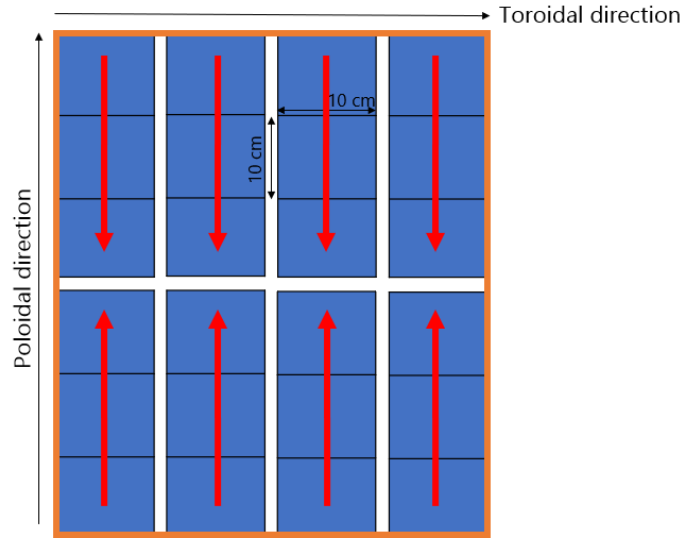


**Figure 43** Proposal 3: 8 parallel paths connecting 3 tiles in series poloidally; each tile is represented by a blue block, while each parallel path is by a red arrow.

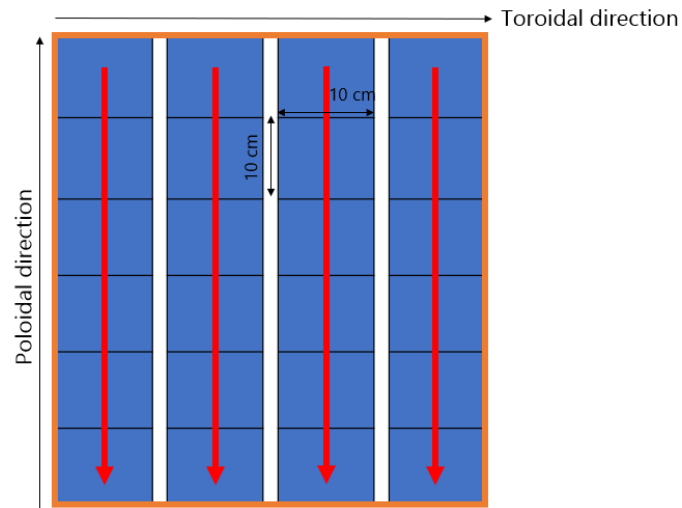


**Figure 44** Proposal 4: 4 parallel paths connecting 6 tiles in series poloidally; each tile is represented by a blue block, while each parallel path is by a red arrow.

## 4.5 Boiling check

All the connection proposals must respect the absence of boiling. Specifically, the absence of boiling is checked by performing conjugate heat transfer analyses on the tile arrays where the major risk is present: the last tile array and a central tile array cooled by the minimum mass flow rate.

To minimize computational costs, symmetry conditions are implemented. Specifically, the size of the last array's inlet manifold is reduced by half, and the inlet and outlet manifolds of the central array are both reduced by half. The inlet mass flow rates are computed on the half-tile PS:

- for the last array from the last outlet section;
- for the central array, from the water mass flow rate distribution in the manifolds. For a better understanding, the water mass flow rate distribution for a  $mfr_{inlet, half-tile\ PS}$  of  $\sim 595\text{ g/s}$  is reported in **Figure 45**: manifold number 5 is the least uncooled with  $mfr_{inlet}$  of  $\sim 56\text{ g/s}$ , to be divided by two.

The inlet mass flow rate values are reported in **Table 3**.

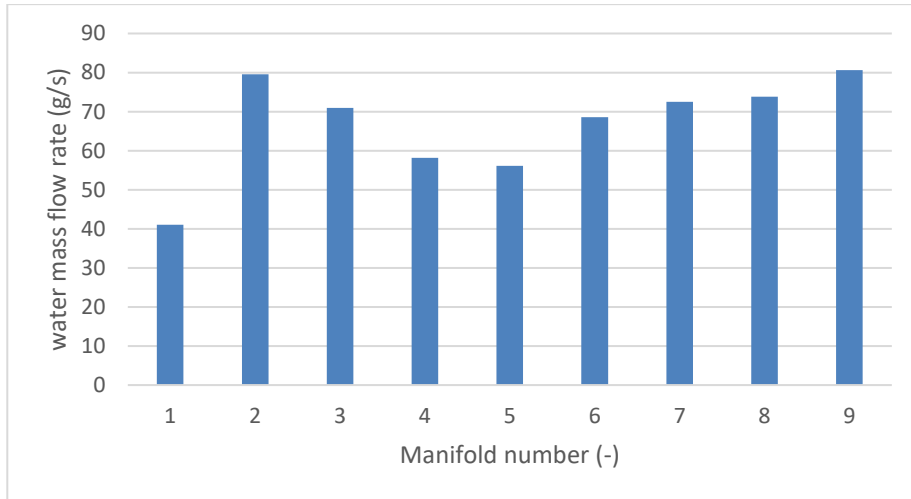


**Figure 45** Water repartitioning, among the manifold, in a half PS tile with an inlet mass flow rate of 595 g/s.

**Table 3** Inlet mass flow rates computed for the last tile array and central tile array.

| $mfr_{inlet}$ (g/s)<br>Half-tile PS | $mfr_{inlet}$ (g/s)<br>Last array | $mfr_{inlet}$ (g/s)<br>Central array |
|-------------------------------------|-----------------------------------|--------------------------------------|
| 500                                 | 43.9                              | 24.1                                 |
| 420                                 | 37.7                              | 20.2                                 |
| 595                                 | 52.2                              | 27.7                                 |

### 4.5.1 Conjugate heat transfer analyses

The thermo-hydraulic simulation setup is the same for the last tile array and the central one; the only difference is concerning the boundary conditions, where the last array has one symmetry plane (inlet manifold surface), while the central one has two symmetry planes (inlet manifold surfaces).

The models used are:

- 3D, steady state
- Turbulence Model K-Omega SST, with all  $y^+$  wall treatment
- Segregated flow
- Segregated fluid temperature
- Segregated solid energy.

The water properties are dependent on the pressure and the temperature, while the galvanized copper and tungsten ones are dependent on temperature.

The following initial conditions are imposed:

- Temperature of the water at the inlet: 27 °C
- Pressure at the outlet: 10 bar.

The following boundary conditions are imposed:

- Fluid inlet surface: inlet mass flow rates taken from **Table 3**
- Fluid outlet surface: pressure outlet
- Manifold cut surface: symmetry plane on the inlet manifold surface (last tile array, **Figure 46**) and on the inlet and outlet manifold surfaces (for the central array **Figure 47**)
- Heated surface: constant heat flux on the tungsten-heated surface.

The mesh implemented is polyhedral with 6 layers of prismatic cells on the fluid (micro-channels and manifold).

The presence of boiling is directly correlated to the difference between the temperature on the MCs wall and the saturation temperature, dependent on the pressure:  $\Delta T_{boiling} = T_{wall} - T_{sat}$ . To avoid boiling,  $\Delta T_{boiling}$  must be negative; in other words, the temperature on the MCs wall must be inferior to the saturation temperature. This computation is performed for the last and central tile arrays,

showing there is no boiling for tiles considered in Proposal 1, Proposal 2 and Proposal 4 imposing a heat flux up to  $10 \text{ MW/m}^2$ , while up to  $14 \text{ MW/m}^2$  in the case of Proposal 3.

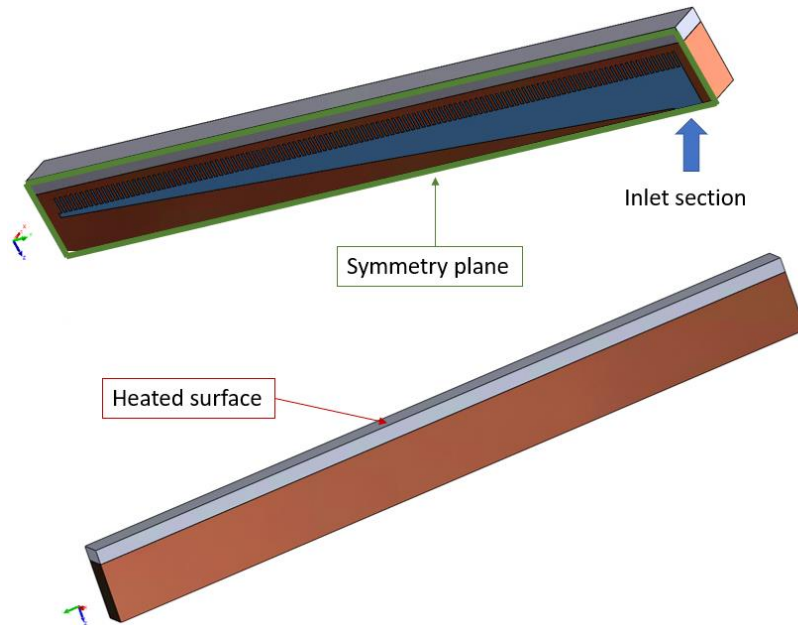


**Figure 46** Last tile array with symmetry plane boundary condition imposed only on the inlet manifold surface.

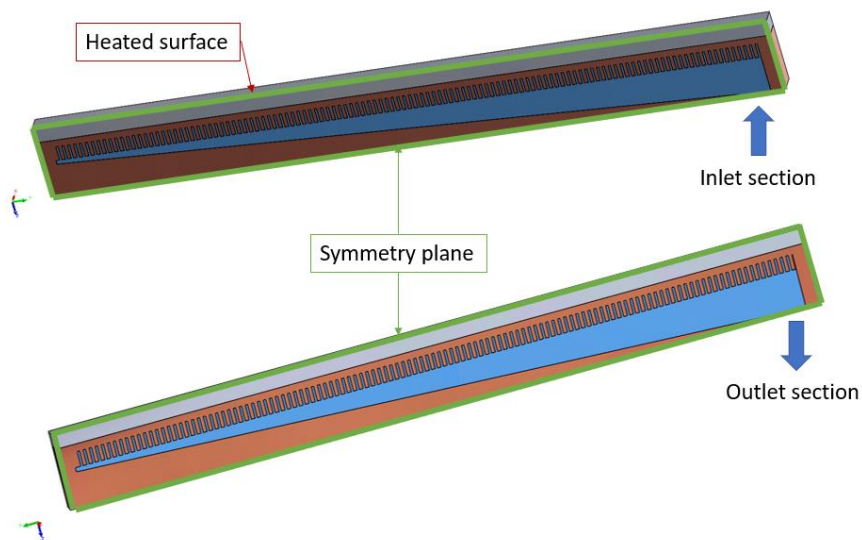


**Figure 47** Central tile array with symmetry plane boundary condition imposed on the inlet manifold and outlet manifold surfaces.

A double check is required for Proposal 1 and Proposal 2 where two tiles are connected in series along the toroidal direction, the same direction on which the maximum heat flux is imposed. In these two cases, the incremental temperature along the previous tile could lead to boiling on the following tile. The incremental temperature is computed from the enthalpy equation (4):

$$\Delta H = c_p \dot{m} \Delta T \quad (4)$$

The enthalpy is computed by multiplying the heat flux ( $10 \text{ MW/m}^2$ ) for the tile surface ( $0.01 \text{ m}^2$ );  $c_p$  is the water specific heat ( $4178.0 \text{ J/kg/K}$ );  $\dot{m}$  is the tile inlet mass flow rate relative to the proposal considered.

The incremental temperatures are:  $\Delta T_{\text{Proposal,1}} \sim 24 \text{ K}$ ,  $\Delta T_{\text{Proposal,2}} \sim 28 \text{ K}$ . As result, the absence of boiling is verified for the Proposal 1, while for the Proposal 2 the incremental temperature leads to boiling. The Proposal 2 can't be taken into consideration anymore.

As an example,  $\Delta T_{\text{boiling}}$  computed on a central array with the  $\text{mfr}_{\text{inlet}}$  of  $27.7 \text{ g/s}$  (taken from **Table 3**) imposing  $14 \text{ MW/m}^2$  as heat flux, is reported in **Figure 48**. Being  $\Delta T < 0 \rightarrow T_{\text{wall}} < T_{\text{sat}}$ , the absence of boiling is verified.

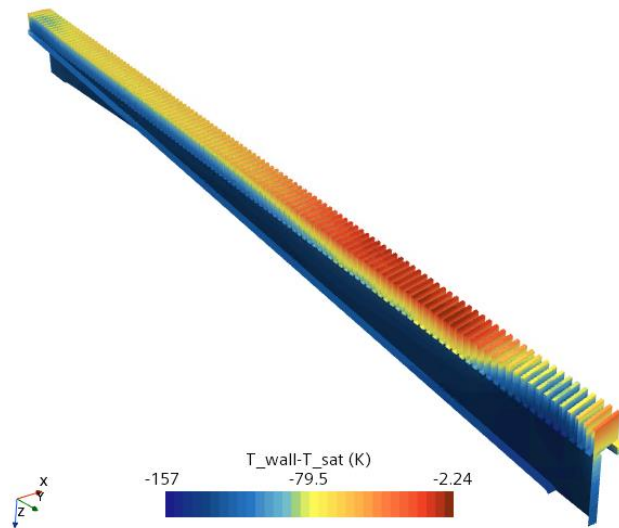


**Figure 48**  $\Delta T_{\text{boiling}} = T_{\text{wall}} - T_{\text{sat}}$  computed on the least uncooled central array with a  $\text{mfr}_{\text{inlet}}$  of  $27.7 \text{ g/s}$  and an imposed heat flux of  $14 \text{ MW/m}^2$  on the heated surface.

## 4.6 Final configuration

According to the previous considerations, **Table 4** summarizes the main results.

The most suitable configuration is Proposal 3, composed of 8 parallel paths connecting poloidally 3 tiles in series. This configuration ensures the single-phase flow for each tile with a maximum heat flux of  $14 \text{ MW/m}^2$ , requiring a total inlet mass flow rate of max  $10 \text{ kg/s}$  and reaching a total pressure drop of  $14.7 \text{ bar}$  ( $0.3 \text{ bar}$  can be considered as a safety factor for minor pressure losses). In this case, a second pump of  $5 \text{ kg/s}$  is necessary. A proposed hydraulic scheme is depicted in **Figure 49**.

**Table 4** Summary of the different tiles connection proposals in a target module; the limits of the infrastructure not respected are highlighted in red.

| Heat flux<br>(MW/m <sup>2</sup> )    | $\dot{m}$ /tile <sup>1</sup><br>(kg/s) | $\Delta p$ /tile<br>(bar) | $\Delta T$ /tile<br>(K) | Proposal number: Tiles connection $N_{\text{parallel}} \times N_{\text{series}}$ |            |            |           |            |            |           |            |            |           |            |            |
|--------------------------------------|--|---------------------------|-------------------------|--|------------|------------|-----------|------------|------------|-----------|------------|------------|-----------|------------|------------|
|                                      |  |                           |                         | P1: 6 x 4  |            |            | P2: 4 x 6 |            |            | P3: 8 x 3 |            |            | P4: 4 x 6 |            |            |
|                                      |  |                           |                         | $\dot{m}$  | $\Delta p$ | $\Delta T$ | $\dot{m}$ | $\Delta p$ | $\Delta T$ | $\dot{m}$ | $\Delta p$ | $\Delta T$ | $\dot{m}$ | $\Delta p$ | $\Delta T$ |
| 10                                   | 0.84                                   | 2.46                      | 28                      |  |            |            | 3.4       | 14.8       | 48         | 6.7       | 7.4        | 28         | 3.4       | 14.8       | 28         |
| 10                                   | 1.00                                   | 3.48                      | 24                      | 6  | 13.9       | 48         |           |            |            |           |            |            |           |            |            |
| 14                                   | 1.19                                   | 4.90                      | 28                      |  |            |            |           |            |            | 9.5       | 14.7       | 28         |           |            |            |
| Current limits of the infrastructure |  |                           |                         | 5  | 15         | 50         | 5         | 15         | 50         | 5         | 15         | 50         | 5         | 15         | 50         |

<sup>1)</sup> Ensuring tile remains in single phase flow

<sup>2)</sup> Presence of boiling on the second tile connected toroidally: this configuration is not applicable.

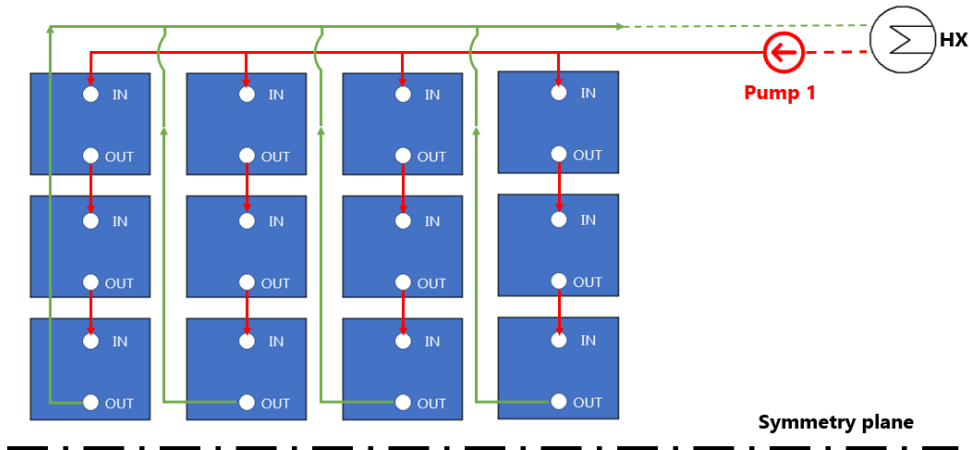


**Figure 49** Hydraulic scheme of Proposal 3 for the TM, composed of 8 parallel paths connecting 3 tiles in series poloidally, requiring two pumps of  $5 \text{ kg/s}$  each; the scheme is represented considering the configuration symmetry.

## Chapter 5

### Conclusions

The aims of the current study are the verification of a lumped model (PS-model) suitability in stresses evaluation, compared to the real model (MCs-model), and the feasibility evaluation of the tiles' hydraulic connection in the target module of the W7-X water-cooled divertor.

To achieve the first one, FEM analyses are carried out to evaluate the interfacial stresses at the bond interface between the plasma-facing tile and the heat sink substrate. The interfacial stresses evaluated are the delamination or peeling and shear stresses since they are responsible for the structural integrity of PFCs. Especially the free surface edge is analyzed, being the most crucial domain where the interfacial stresses reach a peak. After a detailed literature review and FEM analyses on a model with similar geometry to the tile array models considered, MCs and PS arrays are compared, in the elastic regime, with the application of temperature maps extracted from thermo-hydraulic simulations. The comparison shows a very good agreement between the interfacial stresses predicted by the two models; specifically, the stresses at the free edge are overestimated by the PS-array in accordance with the temperature overestimation. This can be considered a safety factor of the lumped model.

Furthermore, a thermo-mechanical application of the lumped model shows how the interfacial stresses decrease with the increase of the thickness between the channel and the bond interface in the heat sink substrate, avoiding the high risk of the interface debonding. In particular, the thickness value of 1 mm is chosen as

most evaluable for the next considerations since it's also compatible with the manufacturing process of the galvanized copper used as heat sink material.

To achieve the second aim, the tile equipped with PS blocks is used to evaluate the pressure drop and the water-manifold distribution relative to different inlet mass flow rates, performing hydraulic analyses. From the water-manifold distribution, the inlet mass flow rate for the least uncooled tile array and the last tile array, being the two tile arrays in the worst condition for the temperature hotspot, are analyzed by performing conjugate heat transfer simulations to verify the single-phase flow. Different hydraulic connections are taken into consideration and the most suitable one prescribes 8 parallel paths connecting poloidally 3 tiles in series, standing up to  $14 \text{ MW/m}^2$  of heat load, but with the installation of a second pump of  $5 \text{ kg/s}$ , since a maximum mass flow rate of  $10 \text{ kg/s}$  is required.

## 5.1 Future perspectives

As the first approach to verify the suitability of the lumped model in stress evaluation, the thermo-mechanical study is performed without considering the cyclic heat load. Future evaluations, such as the thermo-mechanical validation of the designed mockup, must consider the fatigue life of the materials and increase the heat flux up to  $15 \text{ MW/m}^2$ . In this framework, the elastoplastic behavior of the galvanized copper must be implemented. Furthermore, the higher heat flux application requires a new calibration of the lumped model.

Concerning the hydraulic tiles connection, detailed analyses on the entire target module must be performed to verify the preliminary study carried out in this study. Additionally, a further study on the integration of the proposed hydraulic scheme in the complete divertor unit must be done, considering the entire hydraulic circuit and the hydraulic characteristics of the pump.

Finally, the implementation of a soft-copper interlayer between the tungsten and the galvanized copper must be evaluated, since it's generally used as stress relaxing buffer.

# Bibliography

- [1] “Fusion for a cleaner, reliable and self-sufficient energy mix - Fusion for Energy.” <https://fusionforenergy.europa.eu/news/fusion-for-a-cleaner-reliable-and-self-sufficient-energy-mix/> (accessed Mar. 07, 2023).
- [2] “Fusion on Earth - EUROfusion.” <https://euro-fusion.org/fusion/fusion-on-earth/> (accessed Mar. 06, 2023).
- [3] L. Spitzer, “The Stellarator Concept,” *Physics of Fluids*, vol. 1, no. 4, p. 253, 1958, doi: 10.1063/1.1705883.
- [4] “Wendelstein 7-X | Max-Planck-Institut für Plasmaphysik.” <https://www.ipp.mpg.de/w7x> (accessed Mar. 07, 2023).
- [5] T. Klinger *et al.*, “Overview of first Wendelstein 7-X high-performance operation,” *Nuclear Fusion*, vol. 59, no. 11, p. 112004, Nov. 2019, doi: 10.1088/1741-4326/ab03a7.
- [6] H. Renner *et al.*, “The capabilities of steady state operation at the stellarator W7-X with emphasis on divertor design,” *Nuclear Fusion*, vol. 40, no. 6, pp. 1083–1093, Jun. 2000, doi: 10.1088/0029-5515/40/6/306.
- [7] J. Boscary *et al.*, “Design and technological solutions for the plasma facing components of WENDELSTEIN 7-X,” *Fusion Engineering and Design*, vol. 86, no. 6–8, pp. 572–575, Oct. 2011, doi: 10.1016/J.FUSENGDES.2010.11.020.
- [8] J. Boscary *et al.*, “Completion of the production of the W7-X divertor target modules,” *Fusion Engineering and Design*, vol. 166, p. 112293, May 2021, doi: 10.1016/j.fusengdes.2021.112293.
- [9] J. Boscary *et al.*, “Actively Water-Cooled Plasma Facing Components of the Wendelstein 7-X Stellarator,” *Fusion Science and Technology*, vol. 64, no. 2, pp. 263–268, Aug. 2013, doi: 10.13182/FST12-499.

- [10] J. Boscary *et al.*, “Summary of the production of the divertor target elements of Wendelstein 7-X,” *Fusion Engineering and Design*, vol. 124, pp. 348–351, Nov. 2017, doi: 10.1016/j.fusengdes.2017.03.084.
- [11] R. C. Wolf *et al.*, “Performance of Wendelstein 7-X stellarator plasmas during the first divertor operation phase,” *Phys Plasmas*, vol. 26, no. 8, p. 082504, Aug. 2019, doi: 10.1063/1.5098761.
- [12] D. Naujoks *et al.*, “Divertor concept development for the W7-X stellarator experiment,” 2022, Accessed: Mar. 17, 2023. [Online]. Available: <https://publikationen.bibliothek.kit.edu/1000155219>
- [13] H. Ebadi *et al.*, “A multi-scale hybrid approach to the modelling and design of a novel micro-channel cooling structure for the W7X divertor,” *Case Studies in Thermal Engineering*, vol. 42, p. 102734, Feb. 2023, doi: 10.1016/j.csite.2023.102734.
- [14] W. Li, L. Yang, J. Chen, J. Hu, B. Guo, and L. Zhu, “Investigation of the Water Draining Process Pushed by Gas for U-Type and Z-Type Manifolds,” *Science and Technology of Nuclear Installations*, vol. 2022, pp. 1–12, Jan. 2022, doi: 10.1155/2022/5555759.
- [15] S. Kumar Rai and H. Gupta, “REVIEW OF RECENT APPLICATIONS OF MICRO CHANNEL IN MEMS DEVICES,” 2018, Accessed: Mar. 08, 2023. [Online]. Available: <http://www.ripublication.com>
- [16] M. Lu, J. Zhou, and X. Chen, “The Development and Application of Microchannel Heat Sink on W/Cu Flat-Type Mock-Up,” *IEEE Transactions on Plasma Science*, vol. 50, no. 11, pp. 4213–4219, Nov. 2022, doi: 10.1109/TPS.2022.3169809.
- [17] H. Huang, L. Pan, and R. Yan, “Flow characteristics and instability analysis of pressure drop in parallel multiple microchannels,” *Appl Therm Eng*, vol. 142, pp. 184–193, Sep. 2018, doi: 10.1016/j.applthermaleng.2018.06.083.
- [18] L. C. Ruspini, C. P. Marcel, and A. Clause, “Two-phase flow instabilities: A review,” *Int J Heat Mass Transf*, vol. 71, pp. 521–548, Apr. 2014, doi: 10.1016/j.ijheatmasstransfer.2013.12.047.

- [19] Y. K. Prajapati and P. Bhandari, “Flow boiling instabilities in microchannels and their promising solutions – A review,” *Exp Therm Fluid Sci*, vol. 88, pp. 576–593, Nov. 2017, doi: 10.1016/J.EXPTHERMFLUSCI.2017.07.014.
- [20] P. Agostinetti *et al.*, “Investigation of the thermo-mechanical properties of electro-deposited copper for ITER,” *Journal of Nuclear Materials*, vol. 417, no. 1–3, pp. 924–927, Oct. 2011, doi: 10.1016/j.jnucmat.2011.01.084.
- [21] H. Greuner, B. Boeswirth, J. Boscary, and P. McNeely, “High heat flux facility GLADIS:,” *Journal of Nuclear Materials*, vol. 367–370, pp. 1444–1448, Aug. 2007, doi: 10.1016/j.jnucmat.2007.04.004.
- [22] J. H. You and H. Bolt, “Analysis of singular interface stresses in dissimilar material joints for plasma facing components,” *Journal of Nuclear Materials*, vol. 299, no. 1, pp. 1–8, Oct. 2001, doi: 10.1016/S0022-3115(01)00680-8.
- [23] J. H. You and H. Bolt, “Thermal stress intensity factor of interfacial cracks of a plasma facing component under high heat flux loading,” *Fusion Engineering and Design*, vol. 65, no. 4, pp. 483–492, Jul. 2003, doi: 10.1016/S0920-3796(03)00051-6.
- [24] S. Timoshenko, “Analysis of Bi-Metal Thermostats,” *J Opt Soc Am*, vol. 11, no. 3, p. 233, Sep. 1925, doi: 10.1364/JOSA.11.000233.
- [25] E. Suhir, “Interfacial Stresses in Bimetal Thermostats,” *J Appl Mech*, vol. 56, no. 3, pp. 595–600, Sep. 1989, doi: 10.1115/1.3176133.
- [26] D. Post, J. D. Wood, B. Han, V. J. Parks, and F. P. Gerstle, “Thermal Stresses in a Bimaterial Joint: An Experimental Analysis,” *J Appl Mech*, vol. 61, no. 1, pp. 192–198, Mar. 1994, doi: 10.1115/1.2901397.
- [27] J. H. You, H. Bolt, R. Duwe, J. Linke, and H. Nickel, “Thermomechanical behavior of actively cooled, brazed divertor components under cyclic high heat flux loads,” *Journal of Nuclear Materials*, vol. 250, no. 2–3, pp. 184–191, Dec. 1997, doi: 10.1016/S0022-3115(97)00240-7.
- [28] S. Timoshenko, “Analysis of Bi-Metal Thermostats,” *J Opt Soc Am*, vol. 11, no. 3, p. 233, Sep. 1925, doi: 10.1364/JOSA.11.000233.

- [29] C. D. Pionke and G. Wempner, “The Various Approximations of the Bimetallic Thermostatic Strip,” *J Appl Mech*, vol. 58, no. 4, pp. 1015–1020, Dec. 1991, doi: 10.1115/1.2897676.
- [30] E. Suhir, “Thermally Induced Interfacial Stresses in Elongated Bimaterial Plates,” *Appl Mech Rev*, vol. 42, no. 11S, pp. S253–S262, Nov. 1989, doi: 10.1115/1.3152398.
- [31] C. Q. Ru, “Interfacial Thermal Stresses in Bimaterial Elastic Beams: Modified Beam Models Revisited,” *J Electron Packag*, vol. 124, no. 3, pp. 141–146, Sep. 2002, doi: 10.1115/1.1481037.
- [32] J. W. Eischen, C. Chung, and J. H. Kim, “Realistic Modeling of Edge Effect Stresses in Bimaterial Elements,” *J Electron Packag*, vol. 112, no. 1, pp. 16–23, Mar. 1990, doi: 10.1115/1.2904333.
- [33] D. Munz and Y. Y. Yang, “Stress Singularities at the Interface in Bonded Dissimilar Materials Under Mechanical and Thermal Loading,” *J Appl Mech*, vol. 59, no. 4, pp. 857–861, Dec. 1992, doi: 10.1115/1.2894053.
- [34] M. Fränkle, D. Munz, and Y. Y. Yang, “Stress singularities in a bimaterial joint with inhomogeneous temperature distribution,” *Int J Solids Struct*, vol. 33, no. 14, pp. 2039–2054, Jun. 1996, doi: 10.1016/0020-7683(95)00150-6.
- [35] S. Raju, J. D. Whitcomb, and J. G. Goree, “A New Look at-Numerical Analyses of Free-Edge Stresses in Composite Laminates,” Dec. 1980.
- [36] X.-F. Wu and R. A. Jenson, “Stress-function variational method for stress analysis of bonded joints under mechanical and thermal loads,” *Int J Eng Sci*, vol. 49, no. 3, pp. 279–294, Mar. 2011, doi: 10.1016/j.ijengsci.2010.11.005.
- [37] “Getting Started.”  
[https://docs.sw.siemens.com/documentation/external/PL20211129219030255/en-US/userManual/starccmp\\_userguide\\_html/index.html#page/STARCCMP%2FGUID-44BC55FD-ACDE-47F1-A792-C904A5A45CAD.html%23](https://docs.sw.siemens.com/documentation/external/PL20211129219030255/en-US/userManual/starccmp_userguide_html/index.html#page/STARCCMP%2FGUID-44BC55FD-ACDE-47F1-A792-C904A5A45CAD.html%23)  
 (accessed Mar. 24, 2023).

- [38] “ITER organization 2013 ITER technical document, Appendix A, Materials Design Limit Data, SDC-IC, ITER\_D\_222RLN v3.3,” 2013. Accessed: Mar. 24, 2023. [Online]. Available: <https://user.iter.org/default.aspx?uid=23HL7T>

# APPENDIX A: Lumped model accuracy

As described in section 1.3, the lumped model calibration has been conducted applying an heat flux of  $5 \text{ MW/m}^2$  on a subdomain of 6 MCs and the equivalent porous strip; the validation has been further performed on an array with half inlet and outlet manifolds.

The main results are:

- Hydraulic accuracy: the flow repartition along the array among the different MCs or PS is compared and the agreement is very good with a mean error of 9% either with and without the heat load applied on the tungsten surface;
- Thermal accuracy: the average temperature increases (with respect to the water inlet temperature) for the various porous strips and micro-channels along the array are compared and the average relative deviations are 11% for the heated surface.

Since operational constraints impose heat flux values up to  $15 \text{ MW/m}^2$ , the interest is to evaluate hydraulic and thermal accuracy imposing an heat flux on the tungsten surface of  $10 \text{ MW/m}^2$  and  $15 \text{ MW/m}^2$ .

Concerning hydraulic accuracy, there is no relevant difference between the different cases, as visible from **Figure 50**. On the contrary, as shown in **Figure 51**, the thermal accuracy increases applying an heat load of  $10 \text{ MW/m}^2$ , while decreases with an heat load of  $15 \text{ MW/m}^2$ ; the temperature behavior doesn't change in the three cases.

These considerations lead to the conclusion the porous model has been well calibrated and suitable for thermal-hydraulic analyses with an application of heat load up to  $10 \text{ MW/m}^2$ ; a further calibration is necessary in case of heat load higher than  $10 \text{ MW/m}^2$ .

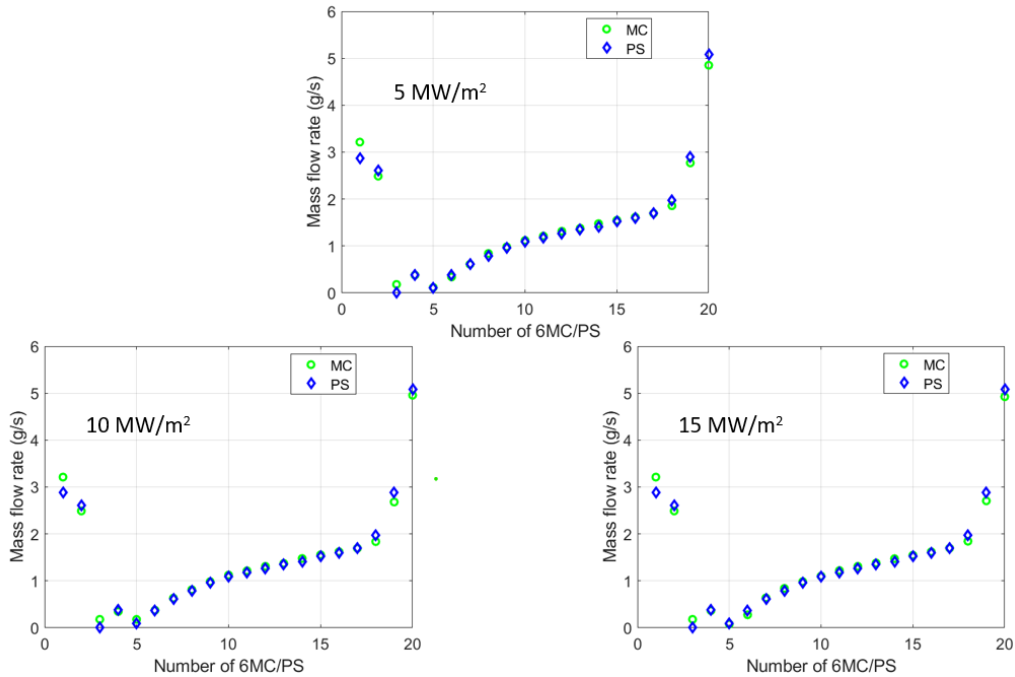


**Figure 50** Mass flow repartition in the different PS and MC (grouped by 6) on a single array with an applied heat load of 5, 10, 15 MW/m<sup>2</sup>, respectively.

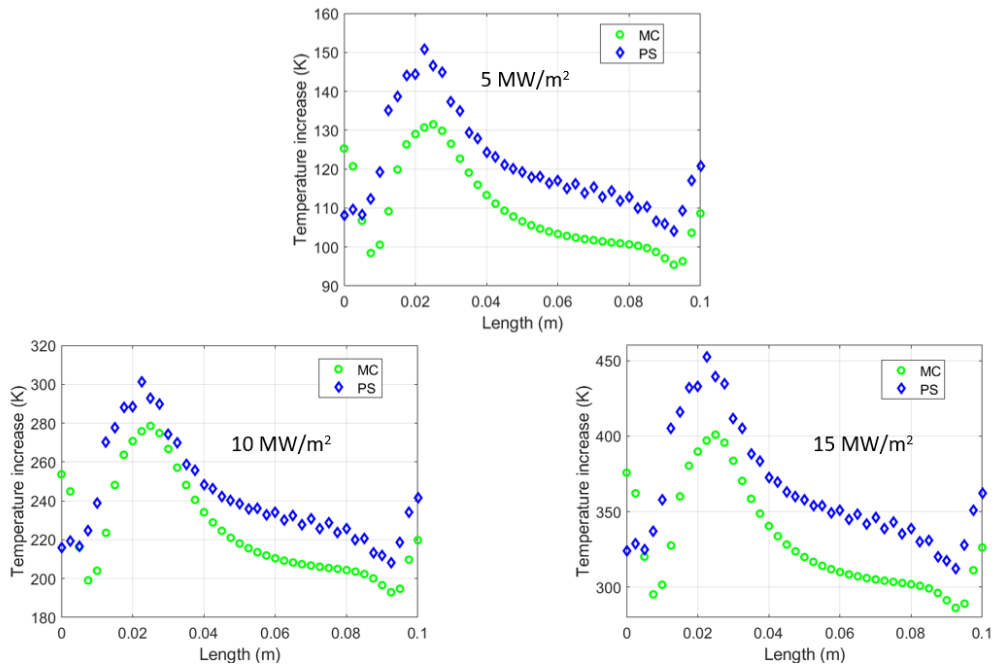


**Figure 51** Average temperature increase (with respect of the inlet water temperature) on the heated surface along a single equipped with MCs and PS, subjected to a heat load of 5, 10, 15 MW/m<sup>2</sup>, respectively.